Moored observations of mesoscale features in the Cape Basin: Characteristics and local impacts on water mass distributions

Marion Kersalé[1,2], Tarron Lamont[1,3], Sabrina Speich[4], Thierry Terre[5], Remi Laxenaire[4], Mike J. Roberts[3,6], Marcel A. van den Berg[3] and Isabelle J. Ansorge[1]

[1]Marine Research Institute, Department of Oceanography - University of Cape Town, Rondebosch, South Africa
[2]Cooperative Institute for Marine and Atmospheric Studies, University of Miami, and NOAA/Atlantic Oceanographic and Meteorological Laboratory, Miami, Florida
[3]Oceans and Coastal Research, Department of Environmental Affairs, South Africa
[4]Laboratoire de Météorologie Dynamique, UMR 8539 École Polytechnique, ENS, CNRS, Paris, France
[5]IFREMER, Univ. Brest, CNRS, IRD, Laboratoire d'Océanographie Physique et Spatiale (LOPS), IUEM, Plouzané, France
[6]Ocean Science & Marine Food Security, Nelson Mandela University, Port Elizabeth, South Africa

Correspondence to: Marion Kersalé (marion.kersale@noaa.gov)

Abstract. The eastern side of the South Atlantic Meridional overturning circulation Basin-wide Array (SAMBA) along the latitude 34.5°S is used to assess the nonlinear, mesoscale dynamics of the Cape Basin. This array presently consists of current meter moorings and bottom mounted Current and Pressure Inverted Echo Sounders (CPIES) deployed across the continental slope. These data, available from September 2014 to December 2015, combined with satellite altimetry allow us to investigate the characteristics and the impact of mesoscale dynamics on local water masses distribution and cross-validate the different data sets. We demonstrate that the moorings are affected by the complex dynamics of the Cape Basin involving Agulhas Rings, cyclonic eddies and anticyclonic eddies from the Agulhas Bank and the South Benguela upwelling front and filaments. Our analyses show that exchange of water masses happens through the advection of water by mesoscale eddies but also via wide water mass intrusions engendered by the existence of intense dipoles. This complex dynamics induces strong intra-seasonal upper-ocean velocity variations and water masses exchanges across the shelf and the open ocean, but also across the subantarctic and subtropical waters. Under three case studies, the full-water column hydrographic properties of each mesoscale feature has been evaluated. This work present the first independent observations comparison between full-depth-moorings and CPIES data sets within the eastern South Atlantic region that gives some evidence of eastern boundary buoyancy anomalies associated with migrating eddies. It also highlights the need to continuously sample the full-water depth as inter-basin exchanges occurs intermittently and affect the whole water column.

1 Introduction

Mesoscale nonlinear dynamics contribute to large-water mass distribution and therefore to the large-scale Meridional Overturning Circulation (MOC) (Gordon, 1985; Biastoch et al., 2008; van Sebille et al., 2012), as they redistribute momentum, heat, and mass between different regions (Robinson, 1983). Nonlinear mesoscale eddies are found throughout the global oceans, but are very energetic when associated with western boundary currents (Chelton et al., 2011). The Agulhas Current, the intense western boundary current of the South Indian Ocean, follows the African shelf edge southwestwards along the east coast. When it reaches the southern tip of Africa, at 34°S, the Agulhas Current lives the continental slope and affected by strong instabilities retroflects at 38°S into the Indian Ocean (Lutjeharms and Cooper, 1996; de Ruijter et al., 1999; Lutjeharms, 2006). These instabilities are responsible for extensive meandering just southwest of South Africa, and shear edge features such as Agulhas rings, eddies and filaments form within this region. These nonlinear, mesoscale features control the Agulhas leakage— defined as the transport of warm and salty Indian Ocean waters into the Atlantic Ocean through the Cape Basin (labeled in Figure 1; e.g., Gordon et al., 1992; de Ruijter et al., 1999). The Agulhas leakage injects buoyancy anomalies that impact the Atlantic MOC (AMOC) strength, and the Atlantic Multi-decadal Oscillation, with a clear implications for climate studies (e.g., Beal et al., 2011; Biastoch et al., 2015).

Agulhas ring observations, collected from shipboard surveys, were first exploited to quantify the energy, heat and salt fluxes of these mesoscale features (e.g., de Ruijter et al., 1999, and references therein). The first inter-ocean exchange estimates were based on individual hydrographic cruise data combined with altimetric tracking of Agulhas rings (Olson and Evans, 1986; Gordon and Haxby, 1990; Duncombe Rae, 1991; van Ballegooyen et al., 1994; Byrne et al., 1995). These combined data revealed the presence of 4 to 8 rings per year propagating into the South Atlantic with speeds ranging between 5 and 10 km day^{-1}, with a diameter up to 400 km and its influence is felt from the surface down to an intermediate depth between 600 and 1100 m. The associated inter-ocean volume transport per ring was estimated between 0.5 and 3 Sv (1 Sv=10^6 m^3 s^{-1}). These first estimates were based on pre-AVISO altimetric statistics and individual ring observations, which led to a large spread of documented volume fluxes estimates. A more accurate estimate of the fluxes in the Cape Basin has been accomplished by deploying a line of instruments across the pathway of Agulhas rings (BEST – Benguela Sources and Transports Experiment: Duncombe Rae et al. (1996); Garzoli and Gordon (1996); Goni et al. (1997)) and deep profiling floats (KAPEX – Cape of Good Hope Experiments: Lutjeharms et al. (1997); Richardson et al. (2003) and MARE – Mixing of Agulhas Rings Experiment – Van Aken et al. (2003)). From these experiments, the northwestward propagation of the rings in the Cape Basin was distinguished through a narrow ring corridor (Garzoli and Gordon, 1996) or through three different routes on the basis of topographic effects (Dencausse et al., 2010). Such measurements have also demonstrated the highly turbulent regime of the Cape Basin and the co-existence of cyclonic and anti-cyclonic eddies which can enhance mixing (Boebel et al., 2003; Matano and Beier, 2003; Richardson and Garzoli, 2003; Hall and Lutjeharms, 2011; Arhan et al., 2011).

The circulation and water mass properties in the Cape Basin region can be greatly affected by nonlinear, mesoscale features associated with the Agulhas leakage. Cyclonic eddies are about 50 km in diameter and are formed along the western coast of

South Africa or inshore of the Agulhas Current (Lutjeharms et al., 2003). Tracked from altimetric data, recirculating plumes of warm water at the sea surface are often described around these eddies. There is a poleward undercurrent that is generally weak to nonexistent in the Cape Basin, except along the continental slope where it can be influenced by deep cyclonic eddies (Richardson and Garzoli, 2003; Baker-Yeboah et al., 2010a). The presence of several Agulhas rings and cyclonic eddies can induce the generation of dipole structures comparable to the Heton model of Hogg and Stommel (1985). These oceanic dipoles have been observed using satellite imagery thanks to their surface signature described as mushroom-like pattern and theoretically described by numerical models in various area focusing on their dynamical characteristics (Ahlnäs et al. 1987; Hooker and Brown, 1994; Hooker et al., 1995; Millot and Taupier-Letage, 2005; Pallàs-Sanz and Viúdez, 2007; Baker-Yeboah et al., 2010b). These counter-rotating eddies enhance horizontal transport of heat along isopycnals, particularly across frontal structures (Spall, 1995) and vertical diapycnal mixing. Related to dipole dynamics, filaments extending well below the thermocline (de Steur et al., 2004) have been observed during hydrographic cruises southwest of Madagascar and in the Cape Basin (de Ruijter et al., 2004; Whittle et al., 2008). Other filaments, originating from the Agulhas Current, have been observed in the South Benguela upwelling frontal zone off the Cape Peninsula in the upper part of the water column (Lutjeharms and Cooper, 1996). They have been associated with a strong equatorward shelf-break front jet, the Cape Peninsula jet (Bang, 1973; Gordon, 1986; Lutjeharms and Meeuwis, 1987; Nelson et al., 1998). This strong equatorward jet can reach a maximum velocity of 1.2 m s^{-1} and its dynamics is suggested to be linked with the local wind forcing during the upwelling season. However, this seasonality is still a subject of discussion as Boyd et al. (1992) show the occurrence of the jet beyond the upwelling season.

Understanding the Cape Basin circulation in the context of this strong nonlinear, mesoscale variability is crucial for many studies. On regional scales, the circulation is important for water mass distribution, local dynamics, ecosystem assessments and air-sea interactions. On large scales, this circulation influences the AMOC and climate. The need of observations in the subtropical South Atlantic at these different scales, led to the establishment of the South Atlantic MOC (SAMOC) international initiative to enhance further observing systems in this area (Garzoli and Matano, 2011). As part of the SAMOC initiative, several efforts to document the inflows of the two main paths of the upper limb of the AMOC have been undertaken across the Drake Passage (e.g., Chereskin et al., 2009; Donohue et al., 2016) and south of South Africa (e. g., GoodHope line - Ansorge et al., 2005; Gladyshev et al., 2008; Speich et al. 2007). A trans-basin AMOC array, South Atlantic MOC Basin-wide Array (SAMBA), which began as a pilot array in 2008-2009 (Speich et al. 2010; Meinen et al., 2013), continues to grow along 34.5°S, a crucial latitude to evaluate the MOC variability and the impact of inter-ocean exchanges (Perez et al., 2011; Schiermeier, 2013). SAMBA is a collaboration between Argentina, Brazil, France, South Africa and the United States, with moorings located on the western and eastern boundaries (Speich et al., 2010; Meinen et al., 2013; Ansorge et al., 2014). Since the pilot deployment described in Meinen et al. (2013), the number of moorings on the boundaries has increased dramatically. The transport and water mass anomalies associated with the deep current and migrating eddies near the western boundary have been well studied (e.g., Meinen et al., 2012, Meinen et al., 2017; Valla et al., submitted, 2018) but the eastern boundary anomalies have not yet been examined along 34.5°S. In the framework of the

SAMOC international project and national programmes (SANAP - South African National Antarctic Programme), our work focuses on the eastern part of the SAMBA array (hereafter SAMBA-east) offering an ideal set of data to observe and characterize mesoscale dynamics—a key link between Indian and Atlantic water exchanges (Figure 1). The analysis of the SAMBA-east moored data sets, from September 2014 to December 2015, provides evidence of mesoscale features passing through the Cape Basin. Experimental evidence of advected mesoscale eddies through moorings line in various parts of the ocean have been presented (Ursella et al., 2011; Sutherland et al., 2011; de Jong et al., 2013) and used to estimate eddy parameters such as their strengths and sizes (Lilly and Rhines, 2002). The main focus of this study is to characterize such mesoscale structures in the Cape Basin region from different data sets obtained along the SAMBA array using the Lilly and Rhines (2002) technique, and to quantify their impact on local water mass distributions.

2 Data and Methods

The eastern part of the SAMBA array during September 2014 to December 2015, consisted of four full depth current meter moorings (hereafter full-depth-moorings), eight Current and Pressure Inverted Echo Sounders (CPIES) and two bottom mounted Acoustic Doppler Current Profiler (ADCP) moorings that were deployed from the shelf to near the Walvis Ridge offshore along 34.5°S (Figure 1). In this study, we will focus on the four full-depth-moorings (hereafter named M1, M2, M3 and M4) extending from the continental shelf edge, at 1121 m of depth, to 15°E, at 4474 m of depth, deployed in September 2014, by the Department of Environmental Affairs (DEA) and the University of Cape Town (UCT), South Africa from the RV *Algoa*, and the four CPIES nearest to the full-depth-moorings (hereafter named P1, P2, P3 and P4), deployed in September 2013, by IFREMER, France and DEA, South Africa from the RV *SA Agulhas II* (Figure 1, Table I).

The characteristics of the moorings and CPIES used in this study are summarized in Table I. All full-depth-moorings (M1-M4) have an upward looking 75kHz RDI ADCP, deployed at the uppermost float at about 400-500 m of depth, set to sample the upper water column at hourly intervals. At selected depths along the mooring lines, SBE 37 MicroCat’s, a high-accuracy conductivity and temperature recorder, were deployed. Some of these instruments also have pressure recorders and optical oxygen sensors, but these sensors will not be used in this study. All of the full-depth-mooring instruments (ADCP and SBE Microcat's) were still recording on recovery, with the exception of two SBE37 MicroCat's that stopped recording, in November 2014, due to low battery power. These two units were both from M4, at depths of 1340 m and 3985 m. The sampling period for the full-depth-mooring instruments was 1h. The collected data were tidally filtered using a second-order Butterworth filter with a 3 day cut-off period. CPIES recorded hourly measurements of round-trip acoustic travel time, bottom pressure, and the velocity at 50 m above the sea-floor. All of the CPIES were recovered and re-deployed, with the exception of P3 which was unfortunately lost during the recovery. Typically, the pressure sensor of the CPIES exhibits either a linear or an exponential plus linear type of drift (Watts and Kontoyiannis, 1990; Donohue et al., 2010; Meinen et al., 2013). After removing the drift following these traditional methods, the same tidal filter has been applied on the CPIES data. The CPIES moorings records were sub-sampled to a daily-averaged value at noon UTC. An empirical lookup table for hydrographic property profiles, known as the "Gravest Empirical Mode" (GEM) method (Meinen and Watts, 2000; Watts et al., 2001) was constructed from 1724 CTD and Argo profiles in the region. These two-dimensional look-up tables of temperature and salinity as functions of depth and travel time are shown in Figure 2-a,b. The scatter between the original hydrographic data and the GEM fields (Figure 2-c,d) provide an estimate of the accuracy. The temperature and salinity scatter is less than 1.5°C and 0.1 psu, respectively. In the deep ocean, the scatter around the GEM field is a larger fraction of the observed variability, however this is because the signals at depth are smaller relative to the noise, and not because the scatter around the GEM field itself is significantly larger. The GEM method has been successfully applied in the eastern South Atlantic (Meinen et al., 2013; Meinen et al., submitted, 2018). Combining the measured τ from the CPIES (Tab. I) with the GEM look-up tables produces daily full-water-column hydrographic profiles. We will primarily look at results from the full-depth moorings (Sections 3.1 - 3.3), and secondarily look at the CPIES moorings (Section 3.4). The set of records presented hereafter were all tidally-filtered as mentioned above.

Following Lilly and Rhines (2002), a set of metrics used to characterize eddies in mooring data were defined. The strength and size of an eddy can be defined by the peak azimuthal velocity (V), the "apparent" radius or half-width of the eddy chord passing by a mooring (X), the temporal center of the eddy (t_0) and of the eddy's influence on the mooring (ΔT). For an advected eddy, the quantification of V needs a separation of the eddy flow from the mean advection flow (magnitude U and direction Θ). The first estimate of V (hereafter V_n) is made maximizing the velocity difference over a time window encompassing the eddy and so giving initial guesses for t_0 and ΔT. This calculation leads to the estimate of the advection direction Θ as the largest velocity is expected in the direction perpendicular to the mean advection flow (direction of V_n). A second measure of V (hereafter V_U) can be obtained by subtracting an estimate of the advecting flow. For this, two methods exist: the "angle" (U_a and Θ_a) and the "filtering" (U_f and Θ_f) techniques. The first method minimizes the angle difference between the observed eddy currents and the observed vertical shear. The second method is useful when the advection flow is large compared to the eddy, and estimates U_f and Θ_f by low-pass filtered velocity time series at the eddy center t_0 using a Hanning window whose length is three times the eddy duration ΔT. More details about these methods can be found in Lilly and Rhines (2002) and the Appendic C of Lilly et al. (2003). For the purpose of this study, the duration of the eddy (ΔT) and the magnitude of the advection flow (U_a and U_f) are used to estimate the "apparent" radius of the eddy: $X = \Delta T \times U$. Finally, the Rossby number can be assessed as $(2\times|V|)/(X\times f)$.

Hydrographic sampling has been conducted along the eastern section of the SAMBA transect during five cruises on board the RV *SA Agulhas II* (September 2013, September 2014, and July 2015) and the RV *Algoa* (September 2014, and December 2015). During each cruise, Conductivity-Temperature-Depth (CTD) casts were carried on at several stations along the transect using multiple SeaBird Electronics SBE 911+ CTD systems and sensors, in order to measure temperature and derive salinity and density. CTDs were conducted from the surface to within 5-10 m of the sea floor on the RV *SA Agulhas II*, with generally five casts offshore (0°E - 15°E) and five casts over the continental slope (15°E-17°E35'). CTDs on the RV *Algoa* were conducted to a maximum depth of 1000 m, with 8 casts over the continental slope (15°E-17°E35') and a sampling resolution of 0.3-0.5° without offshore station. Discrete seawater samples were collected at selected depths for analysis of salinity with a Guildline Portsal salinometer and used for calibration of the CTD conductivity sensors (van den Berg, 2015). The standard deviation of the CTD conductivity and the seawater sample differences were within an envelope of 0.005 wide. Once calibrated, the SBE MicroCat's sensors were attached to the CTD and data was recorded simultaneously at several different depths. When regressed with the CTD temperature and salinity, all the SBE MicroCat's sensors had a root mean square (rms) values greater than 0.9999 for both temperature and salinity. The average standard error for the temperature (salinity) regressions were equal to 0.012 (0.002). Temperature and salinity from CTD casts and SBE MicroCat's sensors were used to calculate conservative temperature [°C] and absolute salinity (S_A [g kg^{-1}]), following the new thermodynamic equation of seawater (IOC et al., 2010).

In addition, satellite imagery was analyzed to give an overview of the surface dynamics in the Cape Basin region. Sea Surface Temperature (SST) was derived from ODYSSEA, a Group for High Resolution Sea Surface Temperature (GHRSST) regional product interpolated on a 0.02° grid for the South African area (Piollé and Autret, 2011; http://cersat.ifremer.fr/data/). The Sea Surface Height (SSH) and geostrophic velocity fields are derived from the Delayed Time Maps of Absolute Dynamic Topography (MADT) mapped daily on a 1/4° Mercator grid (Pujol et al., 2016). An eddy detection method based on the algorithm developed by Chaigneau et al. (2008, 2009) was applied to these ADT fields. This method detects local ADT extremum to identify potential eddy centers and reconstructs the spatially largest closed ADT contour line encompassing each extrema. Only extremum associated to an amplitude (i.e. absolute ADT differences between the extrema and the outermost contour) superior to 1 mm are identified as eddy centers. This criterion is added by Laxenaire et al. (2018, submitted) to prevent the separation of large eddies into two smaller ones. In addition, each eddy was tracked within the boundary of the eddy defined at the previous time step following the method of Pegliasco et al. (2015). This method, based on the low displacement of eddy compared to their size, was modified by Laxenaire et al. (2018, submitted) to take into account both merging and splitting events. In this modified version, no cost function was applied to the eddies in case of multiple association but a minimum of overlapping surface is added. Consequently, splitting events are identified when one eddy is associated to two or more eddies in the next day as well as merging events in the reverse case.

3 Results

3.1 Upper ocean properties and dynamics

To characterize the hydrodynamical properties of the mesoscale features passing through the SAMBA-east array, the measurements of the upward-looking ADCP are analyzed together with concurrent altimetry data.

From September 2014 to December 2015, the mean and the standard deviation of the vertically averaged current magnitude (top 500-700 m of the water column) is between 12.1 ± 7.7 cm s^{-1} at the mooring nearest to the shelf (M1 - blue line, Fig. 3) and 25.5 ± 18.5 cm s^{-1} at the offshore mooring (M4 - red line, Fig. 3). Statistical comparisons between M1-M4 ADCP near-surface velocities recorded at the last bin and the surface geostrophic velocity derived from satellite altimetry have been made (Table II). Typically, the shallowest depth sampled (between 40 and 60 m depth) by the upward-looking ADCP was close to the surface but usually below the Ekman layer (mean value of about 36 m along the section). The comparison has been undertaken mostly in terms of correlation and rms differences between the zonal and meridional components of M1-M4 ADCPs (u_m, v_m) and those from altimetry at the nearest gridded location (u_{alti}, v_{alti}):

$$\Delta V_{rms} = \left[\frac{1}{N} \sum \left[\left(V_m - \overline{V_{m},} \right) - \left(V_{alti} - \overline{V_{alti}} \right) \right]^2 \right]^{1/2} \quad (1)$$

with V the zonal or the meridional components of the velocity and m the index of the mooring. Additionally, comparisons were made by computing the bias (Eq. 2).

$$bias = \overline{V_m} - \overline{V_{alti}} \quad (2)$$

Values of the correlation coefficient between ADCP and altimetry velocity estimates (R) are significant and fell in the range 0.30-0.83 (Table II). To determine the significance of the correlations, the number of independent samples, also known as the number of degrees of freedom (Thomson and Emery, 2014), is estimated by dividing the record length by twice the integral time scale calculated from the variability of each respective quantity (~40 days). The integral time scale is estimated from the integral of the auto-correlation function to its first zero-crossing (see Appendix B in Meinen et al., 2009 for more information). ΔVrms varied from 12.9 to 15.9 cm s-1 (Table II). The absolute values of the biases were typically between 1 and 5 cm s-1, with a maximum of 8.8 cm s-1 at M2. Correlation between the u-component of these velocity measurements showed values greater than 0.7 for the three offshore moorings. Weak correlation coefficients for both components were observed for the mooring closest to the shore (M1, 1121 m of depth). The coefficient for the v-component gradually increases across the continental slope, moving away from the shelf. The correlations for sites away from the shelf are significant considering the mean zonal correlation scales of the satellite product of 150 km at that latitude (Pujol et al., 2016). The poor correlation for both velocity components at M1 can be mainly attributed to its position too close to the coast (~160 km off shore, at the shelf break), and therefore embedded in a different dynamical context than purely geostrophic, and a possible geostrophic shear between the surface and the first level of measurement. The comparisons reveal that satellite data provides a reasonable description of the upper ocean circulation (between 40 and 60 m depth) across the continental slope along our mooring arrays, except near the shelf-break (i.e., well inshore of the 1200 m isobath).

In light of these results, we are confident that the variability of the zonal and meridional components of the upper-layer velocity between 40 and 60 m depth from the offshore moorings (M2 to M4) can be analyzed according to the dynamics inferred from satellite altimetry. Thanks to the eddy detection technique, we can first estimate statistical characteristics of mesoscale eddies passing through the mooring line during the measurement period of the full-depth-moorings along 34.5°S (September, 2014 to December, 2015). A total number of 16 Agulhas rings, defined as anticyclones that enter the Cape Basin crossing the C-line (criteria of Laxenaire et al. (2018, submitted)), is estimated. This line extends from the southernmost tip of Africa (Cape Agulhas) and, after crossing various seamounts, ends at 45°S in the Southern Ocean (Figure 1). From this altimetric tracking, the median radius and standard deviation of these features are equal to 85 ± 43 km (66 ± 38 km considering the solid body rotation). The azimuthal speed of these Agulhas rings is equal to 0.49 ± 0.24 m s^{-1} with a translation speed, mainly northwestward of 11 ± 6 km day^{-1}. Considering our observing system along the SAMBA-east line, 10 anticyclonic and 7 cyclonic eddies influenced the mooring measurements during the ~14 months period of recording at sites M1 (P1) to M4 (P4) (Figure 3, Tab. III). All these mesoscale features passed over one of the mooring and have a closed contour in the satellite dynamic-height amplitude of at least 1 cm. Two of these eddies (anticyclonic A13 and cyclonic C8) were generated at the Agulhas Retroflection and propagated into the Cape Basin through the northern route defined by Dencausse et al. (2010) (green line - Fig. 3). These two eddies have the largest radius compared with other eddies detected in the area (Tab. III). Five of the anticyclonic eddies (A4, A8, A11, A16 and A26) observed in this study are generated by the splitting of an Agulhas ring and four are generated north of the SAMBA line (A2, A12, A24, and A34). The other 6 cyclonic eddies are generated over the slope off the Cape Peninsula.

The currents measured during September 2014-December 2015 in the top 500 m of the water column contain a number of sudden rotational events, seen in the time series of the two velocity components (Figure 4). These transitions in the velocity field are associated with mesoscale eddies passing through the mooring line. The altimetry data allows us to examine the impact of 7 cyclonic (blue shaded areas - Fig. 4) and 10 anticyclonic eddies (red shaded areas - Fig. 4) on zonal and meridional velocity at the four mooring sites. Moreover, the data records show that the presence of dipoles (counter-rotating eddies) affects the velocity measurements (we have observed five of such events: yellow shaded areas - Fig. 4). The presence of dipoles is confirmed in the ODYSSEA SST field by their mushroom-like patterns, the typical surface signature of these features.

To have more of a consistent and complete picture of the mesoscale dynamics in the Cape Basin, the position of these eddies observed by satellite altimetry were analyzed in relation to variations in the ODYSSEA SST field (Figure 5). On September 19, 2014 the eddy identification method detects one cyclonic eddy (C1) and one anticyclonic eddy (A2) close enough to the mooring line to affect the measurements (Fig. 5a).

Approximately one month later (Fig. 5b), C1 is still positioned over M4 and A2 has propagated southeastward. The dipole created by the interaction of these two eddies induces a westward current associated with a warm and relatively wide filament detected at all the moorings (M1-M4).

On December 1, 2014 (Fig. 5c), C1 moves westward still affecting the currents at M4. The generation of anticyclone A8 gives rise to a second dipole with C1, which, again, generates the propagation of a warm filament between these features. On December 19 (Fig. 5d), A8 had merged with A4, an Agulhas ring south of the SAMBA-east line. At that time, a new cyclonic eddy (C7) was generated on the slope, at the South Benguela upwelling front, south of the mooring line.

After two months (Fig. 5e), an anticyclonic eddy (A12) is present between M3 and M4 and a new cyclonic eddy (C9) is generated at 35°S. This cyclonic eddy merges afterwards with an intense cyclonic eddy (C8) coming from the Agulhas retroflection. After the merging, the cyclonic eddies C8 and C9 (called C8) affect the measurements of M2-M3 until the end of March (Fig. 3d). This strong northeastward current is also intensified by an intense cross-shelf density front that is enhanced at that time due to an upwelling event (Fig. 5f) and the northward migration of an Agulhas ring A13 (Fig. 5g). On March 21, 2015, A13 splits to generate A16. This anticyclonic eddy was close enough to M4 to induce the northward propagation of a warm filament on April 3, 2015 (Fig. 5h).

At the end of April, a new dipole is observed due to the interaction of eddies A16 and C14. The cyclonic eddy C14 is generated by the splitting of C8 on April 18, 2015. This intense dipole induced a strong northward current that injected cold surface water across the mooring array in April (Fig. 5i) and warmer Agulhas Current water during the month of May (Fig. 5j,k). This injection of warm water is boosted by the presence of another dipole present around 38°S (C16-A17).

After this intense event, the satellite imagery still reveals the presence of cyclonic eddy C14 in June (Fig. 5k,l) and an anticylonic eddy (A24) in July (Fig. 5m) between M3 and M4. On September 15, 2015 (Fig. 5n), a new dipole (A26, C23) generates a warm filament propagating toward M4. Finally, at the end of this time series, an anticyclonic eddy (A34) and 2 small cyclonic eddies (C23, C25) are observed over the SAMBA line.

In summary, the moorings over the slope (M1, M2 and M3) are affected by six cyclonic eddies and three anticyclonic eddies (Table III, Figures 4 and 5) over the measurement period from September 2014 to December 2015. M1 does not undergo the influence of anticyclonic eddy A13 crossing the SAMBA line more off-shore. The largest velocity perturbations at the upper-slope moorings are associated with cyclonic eddy C8. M4 records show the influence of many anticyclonic eddies compared to the upper-slope moorings and three cyclonic eddies. Largest velocity perturbations are seen at M4 during the presence of the dipole A16 and C14. The presence of these several mesoscale features induce the propagation of four warm filaments and two injections of cold surface water and warmer Agulhas Current water.

3.2 Case studies - Upper water column

From the combined analysis of satellite and mooring data in section 3.2, we selected the period between March and June 2015 to analyze eddy-like features, filaments, and strong intrusions of cold water or Agulhas Current water due to eddy-eddy interactions. We focus on the variability at M4 which exhibits the strongest variations in responses to passing mesoscale features.

Following the method of Lilly and Rhines (2002), the detection of coherent eddies, dipoles or filaments in mooring data can be assessed more quantitatively. The zonal and meridional components of the velocity measured at the mooring can be placed on a hodograph plane (Figure 6a,b,c). In this plane, a combination of a straight line with a segment of a circle (called D-shaped) reflects an eddy structure. The nearer the eddy's center passes close to the mooring, the more the hodograph appears as a straight line. A filament or a front is also characterized by a straight line as for an eddy sliced through its exact center. Eddies can be distinguished from fronts and filaments using progressive vector diagrams (PVD) (Figure 6d,e,f). The eddy structure presents bends unlike fronts or filaments which result in straight lines. Concerning the hodographs for a dipole, it is similar to that of an eddy if one of the cores passes over the mooring. If the mooring measures the velocity in between the two cores, the hodograph shows an impulsive-like feature with strong increase and decrease of the currents.

In accordance to these theoretical points, we have isolated three case studies between March and June 2015. The first case study (Figure 6a,d) illustrate the presence of two anticyclonic eddies, identified as A13 and A16, and one filament between March 9 and April 6, 2015. The D-shape structures on the hodograph (Figure 6a) and the bends to the right associated to anticylonic eddies on the PVD (Figure 6d) appear clearly. To better illustrate these events, the temperature recorded at the first SBE Microcat's demeaned over the time period of each case studies are presented. Within the period during which a positive temperature anomaly associated to the anticyclonic eddies appears in the record, the hodograph tends to be relatively straight. Concerning the filament, it is evident that this feature results in a straight line on both planes (Figure 6a, d). The second hodograph and PVD between May 28 and June 10, 2015 (Figure 6b,e) displays a D-shaped structure and a bend to the left associated with a negative temperature anomaly typical of a cyclonic eddy. According to its time of occurrence, this mesocale feature corresponds to C14. Finally, the final case study between April 8 and May 29, 2015 (Figure 6c,d) exhibits very strong currents with two acceleration and deceleration phases that are associated to a dipole.

Following these three identified cases studies, the vertical–temporal structure of eddy-like features and filaments, and strong intrusions of cold water or Agulhas Current water due to eddy-eddy interactions are analyzed. Moreover, the estimated sizes and strength of eddies (A13, A16 and C14) can be defined (Table IV) according to the Lilly and Rhines (2002) method detailed in Section 2.

Case of Anticyclonic Eddies: From the middle to the end of March (Fig. 7a,b), M4 is impacted by Agulhas rings A13 and A16. The vertical-temporal section of the u- and v-component of the current speed (Fig. 7c,d) shows an eddy-like structures on March 14 and March 24, 2015. The vertical structure of the first Agulhas ring A13 is not evident as it is associated with an advecting flow directed to the southwest (ϴ – Table IV). For the second anticyclonic eddy, A16, the direction of the mean flow shifts toward the west (ϴ – Table IV) and so the eddy-like structure is much clearer in the perpendicular direction (v-component, Fig. 7d). The azimuthal eddy velocities reach 26.0 cm s^{-1} for A13 and 21.7 cm s^{-1} for A16 (V_U – Table IV) from the surface to 200-250m depth. During this period, an increase of temperature (salinity) of 2.4°C (0.3470) is recorded at the SBE37 MicroCat's at 450 m depth (Fig. 7e). We can also evaluate a down-shift of the isopycnal layer of about 200 m for both eddies (Fig. 7f). This quantity is found by interpolating the potential density within the mean vertical profile derived from CTD data. At the end of the time period (April 2), the propagation of a warm filament at the eastern side of A16 was identified (Fig. 5h). The measured v-component of the velocity (Fig. 7d) show at that time a strong northward flow. From the satellite altimetry (colored circles at the top of Fig. 7c,d), the velocity component magnitudes are lower than the ones from the upward-looking ADCP but show similar order changes.

Case of Cyclonic Eddy: The same analysis is undertaken for a second event occurring between May 28 and June 10, 2015. On June 3, 2015 (Fig. 8a), a cyclonic eddy (C14) affects the circulation along the SAMBA line. At this date, the vertical-temporal section of the u-component of the current speed (Fig. 8b) shows an eddy-like structure. During the time period the eddy passes across the mooring, a strong northward advecting flow is recorded (v-component – Fig.8c, ϴ and U– Table IV). The core of this strong cyclonic eddy (-20.0 cm s^{-1} azimuthal velocity) extends from the surface down to 200 m depth. A decrease of salinity and temperature at 500 m depth of 0.13 and 1.71 °C respectively is recorded (Fig. 8d). This decrease can be partly explained by the 100 m uplift of the isopycnal layer at a depth of 500 m (Fig. 8e). From the satellite altimetry (colored circles at the top of Fig. 8b,c), the meridional component of the current speed is in good agreement with the upward-looking ADCP compared to the zonal that shows a lower velocity.

<u>Intrusions - Dipole dynamics:</u> From the end of April to the middle of May (Figure 9), anticyclonic eddy A16 and cyclonic eddy C14 affect the circulation around M4 as a dipole. This intense dipole induces two intense northward pulses of current with meridional velocities exceeding 100 cm s^{-1} on April 22 and May 13 throughout the entire depth of the sampled water column. These two pulses last about 22 and 15 days respectively. Their vertical influence is deeper than 600 m depth. The vertical mooring motion as evidenced by the downward shifts in the range of depths resolved by the ADCP is very intense during these two events. Although depth changes during these events (~ 300 m) were substantial, the minimal variations in pitch and roll (maximum change of 5 and 4 degrees, respectively), were well within accepted limits and indicated that the performance of the mooring is satisfactory. The altimetry data show the same intense northward current at the surface, however there is a pronounced lag of 7 days for the second intrusion. This lag is no longer present if we consider the altimetric velocity one grid eastward (0.25° of resolution). These two pulses of currents impacts the measurements at the first SBE Microcat's sensor (Fig. 9e,f) with large variations of temperature (more than 6°C), salinity (~0.7) and a down-shift of isopycnal layers of about 150-200 m .

3.3 Full water column water masses distribution and variability

We used the daily-averaged temperature and salinity data obtained from SBE37 MicroCat's instruments on moorings to recover the time series of the regional water masses for each mooring. Similar to Lamont et al. (2015), the distribution of water masses was determined according to Conservative Temperature, Absolute Salinity, and density layers, as illustrated in Figure 10a and described in Table V. Modified Upwelled Water (MUW) was defined according to Duncombe Rae (2005) as central shelf water upwelled along the coast and modified due to solar heating and freshwater flux. Oceanic Surface Water (OSW) was defined with the criteria of Donners et al. (2005) as salinity maximum water subducting in the western tropical Atlantic. The criteria of Donners et al. (2005) were also used to define light South Atlantic Central Water (lSACW - defined as Indian Central Water brought into the South Atlantic Ocean by Agulhas Current intrusions), South Atlantic Subtropical Mode Water (SASTMW), and Subantarctic Mode Water (SAMW- with a vertical temperature gradient less than 1.6°C/100 m (Roemmich and Cornuelle, 1992)). Local ventilation of Indian Central waters have been firstly identified by Arhan et al. (2011) inside different sampled Agulhas rings (Arhan et al, 1999; Gladyshev et al., 2008). This water mass has been recently defined in the study of Capuano et al. (2018) as Agulhas Ring Mode Water (ARMW) including in addition to the above two other Agulhas rings previously sampled (Ducombe Rae et al., 1996; McDonagh et al., 1999). Three different varieties of Antarctic Intermediate Water (AAIW), namely Indian AAIW (I-AAIW), Indo-Atlantic AAIW (IA-AAIW) and Atlantic AAIW (A-AAIW) were characterized according to Rusciano et al. (2012). The highest salinity values in the I-AAIW variety are likely associated with Red Sea Intermediate Water (RSIW) which have been shown traveling down the Agulhas current as discontinuous filaments, or confined within anticyclonic and cyclonic eddies (Roman and Lutjeharms, 2007). Upper

Circumpolar Deep Water (UCDW), North Atlantic Deep Water (NADW), and Lower Circumpolar Deep Water (LCDW) were defined according to Heywood and King (2002).

Overall, the vertical distribution of water masses at M4 (colored shaded dots - Fig. 10a) shows that SAMW is present on the southwestern African continental slope around 500 m depth, I-AAIW and IA-AAIW between 500 and 1000 m, UCDW from 1000 to 1500 m depth, NADW between 1600 and 3000 m, and finally LCDW below 3000 m.

The mean vertical and zonal distributions are affected by the regional mesoscale dynamic described in the previous section. Typically a cyclonic (anticyclonic) eddy causes uplift (suppression) of isopycnal layers. The Conservative Temperature and Absolute Salinity relationship is highlighted for these two types of events. During the period of the anticyclonic eddies, the temperature and salinity, and density values at the shallowest SBE Microcat sensor at M4 (red dots - Fig. 10b) show the highest range of values of the all of the time series records. During the time period of the cyclonic eddy, the values are at the opposite end, i.e. the lowest recorded densities (blue dots - Fig. 10b). While the signature of these two features is clearly separated, we do not definitively proves if these changes are associated with a thermohaline anomaly or a simple heave. During the two successive intrusions of waters due to the presence of the dipole at M4, the Conservative Temperature and Absolute Salinity relationship (magenta dots - Fig. 10c) highlights a wide range of values. For this type of event the deepest sensors recorded water masses characteristics different than the ones usually sampled over the time period or the CTD casts (Fig. 10a). The pressure sensor at M4 exhibits the largest vertical variation during the time period of the dipole (Fig. 9c,d). This large vertical mooring motion adds another level of complexity to interpreting this relationship. To understand the origin of these variations, which can be associated to water trapped inside or around the eddies, vertical movement of isopycnal layers and/or mooring motions, the full-water column characteristics will be analyzed with different data sets onto neutral density surfaces.

3.4 Full-water-column analysis – Focus on the 4 case studies

The different data sets allow us to analyze in more detail the effects of the mesoscale features described in the previous sections and successfully cross-validate the measurements made by the different types of moored instruments (full-depth-moorings *vs.* CPIES).

The profiles estimated via the GEM method can be compared with the single point values of temperature and salinity from M4 sensors (8 sensors recording over the common time period, from September 20, 2014 to August 11, 2015). The reconstructed field captures the major changes in temperature and salinity variability in the upper water column. Indeed, significant correlation coefficients between these two independent data sets show values higher than 0.93 for salinity and temperature at the shallowest sensors (~450, 900 m depth). At the deepest levels, the correlation coefficients range between 0.10 and 0.83 and they are not significant at the 95% confidence level. This can be due to the small variability at the deepest levels compared to the scatter around the GEM field (Figure 2).

Measurements from these two data sets are compared for the three case studies described in Section 3.3: the Anticyclonic eddy, the Cyclonic eddy and the dipole. The Conservative Temperature and Absolute Salinity anomalies at M4 due to the presence of the eddies (anticyclone and cyclone: A16 and C14, Fig. 11a,b) and the intrusion of water that arise because of the presence of the dipole (Fig. 11c,d) are calculated relative to the hydrographic properties in “normal conditions” (just before each event occurred).

During the occupancy of A16 at M4, defined as the temporal range from t_0 - 3ΔT to t_0 (Table IV - March 18-24, 2015), the measurements at the SBE37 MicroCat's do not show an increase of temperature or salinity in the water column associated with neutral density larger than 27.3 kg m^{-3} (Fig. 11a,b - red dots). The reconstructed temperature profile via the GEM method in the upper part of the water column captures a maximum of temperature anomaly of 0.21ºC and salinity of 0.06 g kg^{-1} along the 26.6 kg m^{-3} neutral surface (Fig. 11a,b - red line) which is not captured with the single point measurements of the full-depth-mooring. From the measured properties at the SBE37 MicroCat's data, we have evaluated that the changes in temperature and salinity are mostly influenced by the down-shift of the isopycnal layers (Fig. 10b). Negligible anomalies are detected in the deeper part of the water column.

During the time period of C14, defined as before from t_0 - 3ΔT to t_0 (Table IV – May 31 - June 3, 2015), the hydrographic data estimated from the CPIES do not show any anomaly associated with this feature. Indeed, the decrease of temperature and salinity observed is mostly influenced by the up-lift of the isopycnal layers (Fig. 8e). Nevertheless, the shallowest SBE37 MicroCat records warmer and saltier water along the 27.55 kg m^{-3} neutral surface. Anomalies of 0.23ºC for the temperature and of 0.035 g kg^{-1} for the salinity (Fig. 11a,b - blue dots) are characteristics of I-AAIW. However, along this same neutral surface the reconstructed fields from the CPIES do not catch this water mass anomaly. As said before the reconstructed fields from the CPIES are not significantly correlated compared with those of the SBE37 MicroCat's data. Negligible anomalies are detected in the deeper part of the water column.

During the two intrusions of water due to the presence of the dipole (first intrusion: April 11 - 22, 2015; second intrusion: May 7-14, 2015), the temperature and salinity changes for both events (Fig. 11c,d – magenta dots and circles) show large positive anomalies at all neutral densities sampled. As for the cyclonic eddy, during both intrusions the presence of high salinity I-AAIW is observed along the 27.5 kg m^{-3} neutral surface (for example, during the first intrusion, the anomalies are 0.56ºC in temperature and 0.1 g kg^{-1} in salinity). Interestingly from the SBE37 MicroCat's, we observe strong anomalies of temperature and salinity at the lowest neutral surface (~28.13 kg m^{-3}). The presence of such warm (ΔT=+0.37°C) and saltier (ΔS=+0.08 g kg^{-1}) water anomalies at these depths reveal the presence of large pulses of NADW. From the reconstructed CPIES fields, the surface temperature and salinity signatures of the first intrusion (Fig. 11c,d – magenta plain line) show a large negative anomaly at intermediate depth associated, very likely, with water of Subantarctic origins (-0.33ºC for the temperature and -0.09 g kg^{-1} for the salinity along the 26.52 kg m^{-3} neutral surface). During the second intrusion, a warmer (ΔT=+0.42°C) and saltier (ΔS=+0.12 g kg^{-1}) water of Indian origins appears in the upper part of the water column (26.52 kg m^{-3} neutral surface). The combination of both data sets show that these events influence not only the upper layers waters but they also affect most of the water column, down to the bottom.

4 Discussion and concluding remarks

Since 2010, several efforts have been undertaken to enhance further the AMOC observing in the South Atlantic. This strategic monitoring system continues to grow along 34.5°S, a crucial latitude to evaluate the AMOC variability and the impact of inter-ocean exchanges (Drijfhout et al., 2011). As a consequence of the limitations of high spatial and temporal resolution in *in situ* observations, the quantification of inter-ocean exchange is still an ongoing work and many key questions and issues remain open such as what are the characteristics and the impact of mesoscale structures on local water masses exchange and distribution. In the framework of the SAMOC initiative, we provide here further investigation using a combination of satellite altimetry, full-depth-moorings measurements and CPIES records.

Focusing on the SAMBA-east array, the general circulation around South Africa has been rather well described in previous studies. Two main processes have been observed to influence this area: an equatorward shelf-break frontal jet off the Cape Peninsula (Lutjeharms and Meeuwis, 1987; Nelson et al., 1998) and the instabilities of the Agulhas Current responsible for the spawning of mesoscale eddies propagating into the Cape Basin (Lutjeharms and Cooper, 1996; de Ruijter et al., 1999; Lutjeharms, 2006).

During the time period of our study (~14 months), we objectively identified from satellite altimetry 16 anticyclonic eddies as Agulhas rings. The eddy statistics (diameter of 170 ± 86 km with translation speeds of 11 ± 6 km day^{-1}) are in good agreement with previous estimates (diameter of 200-400 km – *e.g.* Arhan et al, 1999; translation speed of 2.9-7.3 km day^{-1} *e.g.* Olson and Evans, 1986; Byrne et al., 1995; Goni et al. 1997; Schouten et al. 2000). The comparisons reveal that satellite data provides a reasonable description of the upper ocean circulation along the continental slope at our mooring locations, except near the shelf-break (i.e., along and inshore of the 1200 m isobath).

Analyses of both satellite and mooring data show that the eastern mooring array is strongly affected by the intense regional mesoscale variability. Previous studies (Arhan et al., 1999, 2011; Schouten et al., 2000; Boebel et al., 2003) have shown that Agulhas rings coexist with cold-core (cyclonic) eddies, which can contribute directly to the input of Indian water in the Atlantic (Lutjeharms et al., 2003; Arhan et al., 2011; Capuano et al., 2018). The resulting interaction of cyclonic and anticyclonic eddies can be also responsible for the extraction of warm Agulhas water filaments (Lutjeharms and Cooper, 1996; Whittle et al., 2008). These filaments may provide not more than 15% of the total mass flux of Indian Ocean waters into the South Atlantic (Lutjeharms and Cooper, 1996).

Over the measurement period from September 2014 to December 2015, the slope moorings (M1, M2 and M3) show to be affected essentially by cyclonic eddies of different origins. Indeed, these moorings are affected by one cyclonic eddy generated at the Agulhas Bank (C8), one from the splitting of the later (C14) and four along the South Benguela upwelling front. The off-shore mooring (M4) is affected by the more complex dynamics characterizing the Cape Basin involving 6 Agulhas Rings, and cyclonic/anticyclonic eddies both generated along the South Benguela upwelling front. The propagation of four warm surface filaments have been highlighted. The presence of these several mesoscale features induce intense intra-seasonal upper-ocean velocity variations and water masses exchanges across both, the shelf and the open ocean and between the subantarctic and the subtropical frontal zones.

Our study indicates that exchanges of water masses across the continental slope happen through water advection not only via mesoscale eddies but also wide filaments engendered by the interaction among eddies, and in particular, through the existence of intense dipoles. As illustrated in previous studies, such filaments can extend well in to the thermocline and can be related to dipole dynamics (de Steur et al., 2004; Baker-Yeboah et al., 2010b). These wide intrusions cause intense north-northwestward currents affecting the whole water column. These injections are different from ordinary filaments, which exhibit a much smaller vertical extension (around 300 m of the water column). Among the different processes observed along the SAMBA-east array, the most significant event is the intrusion of waters of Indian Ocean and subantarctic origin due to the presence of intense dipoles.

In terms of number of occurrence of each type of event during the 14 months of record, we account for two intrusions of waters associated with the presence of a dipole, six Agulhas rings, seven cyclonic eddies, four anticyclonic eddies and four warm filaments. Our work suggests that not only the advection of water within Agulhas rings or cyclonic eddies is important but that also dipole intrusions and filaments have a significant impact on the total mass, heat, and salt fluxes and therefore, they all need to be better accounted for.

The presence of cyclonic eddies, filaments and interaction of cyclonic and anticyclonic eddies have been also described in more detail in this study with our three case studies. Following the Lilly and Rhines (2002) method, an assessment of coherent eddies, dipoles and filaments in mooring data have been achieved. This method allowed us to evaluate the eddy parameters, such as the eddy apparent radius, the direction of the mean flow, and the Rossby number, all essential elements to characterize eddies in a single point measurements. The estimation of small Rossby number associated to these features reveals that the momentum equation is dominated by the geostrophic balance between the pressure gradient and the Coriolis forces. This quantification implies that altimetry data is adequate for investigating the dynamics of the observed mesocale features. From altimetry data, these eddies have an azimuthal velocity exceeding their translation speed, confirming their non-linear nature and so their ability to advect a parcel of trapped fluid as they translate.

During the first two case studies, the typical impact of cyclonic and anticyclonic eddies causing, respectively, an uplift and downward motion of isopycnal layers are revealed. For the dipole case study, a downward motion of ispoycnal layers is recorded associated with a vertical movement of the mooring.

The different properties of each event have been compared between full-depth-moorings and CPIES measurements in density space allowing a better characterization of the full-water column hydrographic properties and the opportunity to distinguish the changes of temperature and salinity due to vertical motion (isopycnal and/or mooring displacement) versus trapped water masses. In the upper part of the water column, the presence of Indian water trapped inside the Agulhas rings or advected within dipoles have been identified thanks to the reconstructed field. The intrusion of subantarctic water in the upper water layers due to the dipole dynamics is also highlighted. Associated with these upper intrusions of Indian and subantarctic waters due to the presence of dipoles, high-salinity I-AAIW at intermediate depth and NADW at the deepest level are also illustrated. The presence of intermediate high-salinity I-AAIW is also evidenced during the period of the cyclonic eddies crossing.

It has been shown that the trapping depth of rings can reach the sea floor (Van Aken et al., 2003). This influence can even reach the deepest water layers. Indeed, the analyses of our tall mooring deep SBE MicroCat data show that not only Agulhas ring but also water intrusions due to presence of dipoles extend to 4400 m of depth impacting the NADW layers and even deeper layers.

This study presents the first combination of full-depth-moorings and CPIES data sets and supports the interest of the reconstructed field with the GEM technique in the upper water column within the eastern South Atlantic region. Here properties are well resolved by the combination of local sensors and by the GEM reconstructed fields. The reconstructed fields capture the major changes of the temperature and salinity variability in the upper water column associated with inflows of subantarctic or Indian waters. These typical upper water mass characteristics can not be distinguished with the local sensors in our case studies. This can be attributed to the limited vertical sampling resolution in the upper 500 m, and the mixing associated with the mesoscale activity in the Cape Basin which can result in substantial uplift and downwelling of waters. However, the deep-water column properties remain to be analyzed with local temperature and salinity sensors. Moreover, the distance between CPIES and full-depth-moorings (*e.g.* 210 km between M3 and M4) unables precise transport estimates - as the typical velocity decorrelation length scale is smaller than this distance (~100 km – e.g., Donohue et al., 2010; Meinen et al., 2017).

Finally, this work present the first independent observations comparison between full-depth-moorings and CPIES data sets along the SAMBA-east array that gives some evidence of eastern boundary buoyancy anomalies associated with migrating eddies. It also highlights the need to continuously sample the full-water depth as inter-basin exchanges occurs intermittently and affect the whole water column. Future investigations with longer time series at these existing sites will lead to a better understanding of the eastern boundary current variability and Indo-Atlantic exchanges. The impact of each isolated mesoscale eddies will not be adequately resolved at this scale but the global eddy thickness flux anomalies can be improved. The CPIES records used in combination with the moored instruments in the western part of the SAMBA array will improve of our understanding of the strength and variability of the AMOC.

Acknowledgment. The authors would like to express their great appreciation to the Captain, officers and crew of the research vessels, which have supported this program to date, including the South African research vessels the RV *Algoa*, and the RV *SA Agulhas II*. We are warmly grateful to the technical staff who worked on the preparation, deployment and the recovery of the instruments. And our thanks to those who have helped coordinate these challenging international cruise collaborations. The authors acknowledge the support of grants from NRF/SANAP – SAMOC-SA programme. MK acknowledges support from a NRF grant via a South-African post-doctoral fellowship. MK work on this study was carried out in part under the auspices of the Cooperative Institute for Marine and Atmospheric Studies (CIMAS), a Cooperative Institute of the University of Miami and the National Oceanic and Atmospheric Administration (NOAA), cooperative agreement NA10OAR4320143. MK also acknowledges support from the NOAA Atlantic Oceanographic and Meteorological Laboratory. This work was also supported by the European Union's Horizon 2020 research and innovation programme under grant agreement no. 633211 (AtlantOS) and the 11- ANR-56-004 grant for SS. Users can access the CPIES data available at LOPS from T. Terre (thierry.terre@ifremer.fr). Data from the hydrographic casts and the full-depth-moorings can be available at DEA from T. Lamont (tarron.lamont@gmail.com) under certain data sharing policies. The altimeter products were produced by Ssalto/Duacs and distributed by Aviso, with support from CNES (http://www.aviso.oceanobs.com/duacs/). The authors thank Renellys C. Perez, Chris S. Meinen and Jonathan Lilly for precious help, comments and useful discussions. Finally, we thank the three reviewers of this manuscript for their constructive comments.

References

Ahlnäs, K., Royer, T. C., & George, T. H. (1987). Multiple dipole eddies in the Alaska Coastal Current detected with Landsat thematic mapper data. J. Geophys. Res., 92(C12), 13041-13047, doi: 10.1029/JC092iC12p13041.

Ansorge, I. J., Speich, S., Lutjeharms, J. R. E., Goni, G. J., Rautenbach, C. D. W., Froneman, P. W., Rouault, M. and Garzoli, S. (2005). Monitoring the oceanic flow between Africa and Antarctica: report of the first GoodHope cruise: research in action. S. Afr. J. Sci., 101(1-2), 29-35.

Ansorge, I. J., Baringer, M. O., Campos, E. J. D., Dong, S., Fine, R. A., Garzoli, S. L., Goni, G., Meinen, C. S., Perez, R. C., Piola, A. R., Roberts, M. J., Speich, S., Sprintall, J., Terre, T. and Van den Berg, M. A. (2014). Basin-Wide Oceanographic Array Bridges the South Atlantic. Eos, Transactions American Geophysical Union, 95(6), 53-54, doi:10.1002/2014EO060001.

Arhan, M., Mercier, H. and Lutjeharms, J. R. E. (1999). The disparate evolution of three Agulhas rings. J. Geophys. Res., 104(C9), 20987-21005, doi:10.1029/1998JC900047.

Arhan, M., Speich, S., Messager, C., Dencausse, G., Fine, R. and Boye, M. (2011). Anticyclonic and cyclonic eddies of subtropical origin in the subantarctic zone south of Africa. J. Geophys. Res., 116(C11), doi:10.1029/2011JC007140.

Baker-Yeboah, S., Byrne, D. A. and Watts, D. R. (2010a). Observations of mesoscale eddies in the South Atlantic Cape Basin: Baroclinic and deep barotropic eddy variability. J. Geophys. Res., 115(C12), doi:10.1029/2010JC006236.

Baker-Yeboah, S., Flierl, G. R., Sutyrin, G. G. and Zhang, Y. (2010b). Transformation of an Agulhas eddy near the continental slope, Ocean Sci., 6, 143-159, doi:10.5194/os-6-143-2010.

Bang, N. D. (1973). Characteristics of an intense ocean frontal system in the upwell regime west of Cape Town. Tellus, 25(3), 256-265, doi: 10.3402/tellusa.v25i3.9659.

Beal, L. M., De Ruijter, W. P., Biastoch, A. and Zahn, R. (2011). On the role of the Agulhas system in ocean circulation and climate. Nature, 472(7344), 429-436, doi:10.1038/nature09983.

Biastoch, A., Böning, C. W. and Lutjeharms, J. R. E. (2008). Agulhas Leakage dynamics affects decadal variability in Atlantic overturning circulation. Nature, 456, 489–492, doi: 10.1038/nature07426.

Biastoch, A., Durgadoo, J. V., Morrison, A. K., Van Sebille, E., Weijer, W. and Griffies, S. M. (2015). Atlantic multi-decadal oscillation covaries with Agulhas leakage. Nature, 6, 10082, doi: 10.1038/ncomms10082.

Boebel, O., Lutjeharms, J., Schmid, C., Zenk, W., Rossby, T. and Barron, C. (2003). The Cape Cauldron: a regime of turbulent inter-ocean exchange. Deep Sea Res., Part II, 50(1), 57-86, doi: 10.1016/S0967-0645(02)00379-X.

Boyd, A. J., Taunton-Clark, J. and Oberholster, G. P. J. (1992). Spatial features of the near-surface and midwater circulation patterns off western and southern South Africa and their role in the life histories of various commercially fished species. Afr. J. Mar. Sci., 12(1), 189-206, doi: 10.2989/02577619209504702.

Byrne, D. A., Gordon, A. L. and Haxby, W. F. (1995). Agulhas eddies: A synoptic view using Geosat ERM data. J. Phys. Oceanogr., 25(5), 902-917, doi: 10.1175/1520-0485(1995)025<0902:AEASVU>2.0.CO;2.

Capuano, T. A., Speich, S., Carton, X. and Blanke, B. (accepted, 2018). Mesoscale and Submesoscale Processes in the Southeast Atlantic and Their Impact on the Regional Thermohaline Structure. J. Geophys. Res., doi: 10.1002/2017JC013396.

Chaigneau, A., Gizolme, A. and Grados, C. (2008). Mesoscale eddies off Peru in altimeter records: Identification algorithms and eddy spatio-temporal patterns. Prog. Oceanogr., 79(2), 106-119, doi: 10.1016/j.pocean.2008.10.013.

Chaigneau, A., Eldin, G. and Dewitte, B. (2009). Eddy activity in the four major upwelling systems from satellite altimetry (1992–2007). Prog. Oceanogr., 83(1-4), 117-123, doi:10.1016/j.pocean.2009.07.

Chelton, D. B., Schlax, M. G., & Samelson, R. M. (2011). Global observations of nonlinear mesoscale eddies. Prog. Oceanogr., 91(2), 167-216, doi: 10.1016/j.pocean.2011.01.002.

Chereskin, T. K., Donohue, K. A., Watts, D. R., Tracey, K. L., Firing, Y. L. and Cutting, A. L. (2009). Strong bottom currents and cyclogenesis in Drake Passage. Geophys. Res. Lett., 36(23), doi: 10.1029/2009GL040940.

De Steur, L., Van Leeuwen, P. J., & Drijfhout, S. S. (2004). Tracer leakage from modeled Agulhas rings. J. Phys. Oceano., 34(6), 1387-1399, doi:10.1175/1520-0485(2004)034<1387:TLFMAR>2.0.CO;2.

Dencausse, G., Arhan, M. and Speich, S. (2010). Routes of Agulhas rings in the southeastern Cape Basin. Deep Sea Res., Part I, 57(11), 1406-1421, doi: 10.1016/j.dsr.2010.07.008.

Donners, J., Drijfhout, S. S. and Hazeleger, W. (2005). Water mass transformation and subduction in the South Atlantic. J. Phys. Oceano., 35(10), 1841-1860, doi: 10.1175/JPO2782.1.

Donohue, K. A., Watts, D. R., Tracey, K. L., Greene, A. D. and Kennelly, M. (2010). Mapping circulation in the Kuroshio Extension with an array of current and pressure recording inverted echo sounders. J. Atmos. Oceanic Technol., 27(3), 507-527, doi:10.1175/2009JTECHO686.1.

Donohue, K. A., Tracey, K. L., Watts, D. R., Chidichimo, M. P. and Chereskin, T. K. (2016). Mean Antarctic Circumpolar Current transport measured in Drake Passage. Geophys. Res. Lett., 43, 11,760–11,767, doi: 10.1002/2016GL070319.

Drijfhout, S. S., Weber, S. L. and van der Swaluw, E. (2011). The stability of the MOC as diagnosed from model projections for pre-industrial, present and future climates, Clim. Dyn., 37, 1575-1586, doi:10.1007/s00382-010-0930-z.

Duncombe Rae, C. M. (1991). Agulhas retroflection rings in the South Atlantic Ocean: an overview. Afr. J. Mar. Sci., 11(1), 327-344, doi: 10.2989/025776191784287574.

Duncombe Rae, C. M., Garzoli, S. L. and Gordon, A. L. (1996). The eddy field of the southeast Atlantic Ocean: A statistical census from the Benguela Sources and Transports Project. J. Geophys. Res., 101(C5), 11949-11964, doi: 10.1029/95JC03360.

Duncombe Rae, C. M. (2005). A demonstration of the hydrographic partition of the Benguela upwelling ecosystem at 26°40'S. Afr. J. Mar. Sci., 27(3), 617-628, doi: 10.2989/18142320509504122.

Garzoli, S. L. and Gordon, A. L. (1996). Origins and variability of the Benguela Current. J. Geophys. Res., 101(C1), 897-906, doi: 10.1029/95JC03221.

Garzoli, S. L., and Matano, R. (2011). The South Atlantic and the Atlantic meridional overturning circulation. Deep Sea Res., Part II, 58(17), 1837-1847, doi: 10.1016/j.dsr2.2010.10.063.

Gladyshev, S., Arhan, M., Sokov, A. and Speich, S. (2008). A hydrographic section from South Africa to the southern limit of the Antarctic Circumpolar Current at the Greenwich meridian. Deep Sea Res., Part I, 55(10), 1284-1303, doi: 10.1016/j.dsr.2008.05.009.

Goni, G. J., Garzoli, S. L., Roubicek, A. J., Olson, D. B. and Brown, O. B. (1997). Agulhas ring dynamics from TOPEX/POSEIDON satellite altimeter data. J. Mar. Res., 55(5), 861-883, doi: 10.1357/0022240973224175.

Gordon, A. L. (1985). Indian-Atlantic transfer of thermocline water at the Agulhas Retroflection. Science, 227, 1030-1033, doi: 10.1126/science.227.4690.1030.

Gordon, A. L. (1986). Interocean exchange of thermocline water. J. Geophys. Res., 91, 5037–5046, doi: 10.1029/JC091iC04p05037.

Gordon, A. L. and Haxby, W. F. (1990). Agulhas eddies invade the South Atlantic: Evidence from Geosat altimeter and shipboard conductivity‐temperature‐depth survey. J. Geophys. Res., 95(C3), 3117-3125, doi: 10.1029/JC095iC03p03117.

Gordon, A. L., Weiss, R. F., Smethie, W. M. and Warner, M. J. (1992). Thermocline and intermediate water communication between the South Atlantic and Indian Oceans. J. Geophys. Res., 97(C5), 7223-7240, doi: 10.1029/92JC00485.

Hall, C. and Lutjeharms, J. R. E. (2011). Cyclonic eddies identified in the Cape Basin of the South Atlantic Ocean. J. Mar. Syst., 85(1), 1-10, doi: 10.1016/j.jmarsys.2010.10.003.

Heywood, K. J. and King, B. A. (2002). Water masses and baroclinic transports in the South Atlantic and Southern oceans. J. Mar. Res., 60(5), 639-676, doi: 10.1357/002224002762688687.

Hogg, N. G. and Stommel, H. M. (1985). The heton, an elementary interaction between discrete baroclinic geostrophic vortices, and its implications concerning eddy heat-flow. In Proceedings of the Royal Society of London A: Mathematical, Physical and Engineering Sciences (Vol. 397, No. 1812, pp. 1-20). The Royal Society.

Hooker, S. B. and Brown, J. W. (1994). Warm core ring dynamics derived from satellite imagery. J. Geophys. Res., 99(C12), 25181-25194, doi: 10.1029/94JC02171.

Hooker, S. B., Brown, J. W., Kirwan, A. D., Lindemann, G. J., & Mied, R. P. (1995). Kinematics of a warm‐core dipole ring. J. Geophys. Res., 100(C12), 24797-24809, doi: 10.1029/95JC02900.

IOC, Scor, IAPSO, 2010. The International Thermodynamic Equation of Seawater 2010: Calculation and Use of Thermodynamic Properties. Intergovernmental Oceanographic Commission, Manuals and Guides No. 56.

de Jong, M. F., Bower, A. S. and Furey, H. H. (2014). Two years of observations of warm-core anticyclones in the Labrador Sea and their seasonal cycle in heat and salt stratification. J. Phys. Oceanogr., 44(2), 427-444, doi: 10.1175/JPO-D-13-070.1.

Lamont, T., Hutchings, L., Van Den Berg, M. A., Goschen, W. S. and Barlow, R. G. (2015). Hydrographic variability in the St. Helena Bay region of the southern Benguela ecosystem. J. Geophys. Res., 120(4), 2920-2944, doi: 10.1002/2014JC010619.

Laxenaire, R., Speich, S., Blanke, B., Chaigneau, A. and Pegliasco, C. (submitted, 2018). Agulhas Ring trajectories connecting western boundaries as inferred from altimetry. J. Geophys. Res. Ocean.

Lilly, J. M. and Rhines, P. B. (2002). Coherent eddies in the Labrador Sea observed from a mooring. J. Phys. Oceanogr., 32(2), 585-598, doi:10.1175/1520-0485(2002)032<0585:CEITLS>2.0.CO;2.

Lilly, J. M., Rhines, P. B., Schott, F., Lavender, K., Lazier, J., Send, U. and D'Asaro, E. (2003). Observations of the Labrador Sea eddy field. Prog. Oceanogr., 59(1), 75-176, doi:10.1016/j.pocean.2003.08.013.

Lutjeharms, J. R. E. and Meeuwis, J. M. (1987). The extent and variability of South-East Atlantic upwelling. Afr. J. Marine Sci., 5(1), 51-62, doi: 10.2989/025776187784522621.

Lutjeharms, J. R. E. and Cooper, J. (1996). Interbasin leakage through Agulhas Current filaments. Deep Sea Res., Part I, 43(2), 213217-215238, doi: 10.1016/0967-0637(96)00002-7.

Lutjeharms, J. R. E., Boebel, O. and Rossby, T. (1997). KAPEX: an international experiment to study deep water movement around southern Africa. S. Afr. J. Sci., 93, 377-381.

Lutjeharms, J. R. E., Boebel, O. and Rossby, H. T. (2003). Agulhas cyclones. Deep Sea Res., Part II, 50(1), 13-34, doi: 10.1016/S0967-0645(02)00378-8.

Lutjeharms, J. R. E. (2006). The Agulhas Current. Springer Berlin Heidelberg, 329pp, doi:10.1007/3-540-37212-1.

Matano, R. P., & Beier, E. J. (2003). A kinematic analysis of the Indian/Atlantic interocean exchange. Deep Sea Res., Part II, 50(1), 229-249, doi: 10.1016/S0967-0645(02)00395-8.

McDonagh, E. L., Heywood, K. J. and Meredith, M. P. (1999). On the structure, paths, and fluxes associated with Agulhas rings. *J. Geophys. Res.*, *104*(C9), 21007-21020, doi:10.1029/1998JC900131.

Meinen, C. S and Watts, D. R. (2000). Vertical structure and transport on a transect across the North Atlantic Current near 42°N: Time series and mean. J. Geophys. Res., 105(C9), 21869-21891, doi: 10.1029/2000JC900097.

Meinen, C. S., Luther, D. S. and Baringer, M. O. (2009). Structure, transport and potential vorticity of the Gulf Stream at 68° W: Revisiting older data sets with new techniques. Deep Sea Res., Part I, 56(1), 41-60, doi:10.1016/j.dsr.2008.07.010.

Meinen, C. S., Piola, A. R., Perez, R. C. and Garzoli, S. L. (2012). Deep Western Boundary Current transport variability in the South Atlantic: preliminary results from a pilot array at 34.5° S. Ocean Sci., 8(6), 1041-1054, doi: 10.5194/os-8-1041-2012.

Meinen, C. S., Speich, S., Perez, R. C., Dong, S., Piola, A. R., Garzoli, S. L., Baringer, M. O., Gladyshev, S. and Campos, E. J. D. (2013), Temporal variability of the meridional overturning circulation at 34.5ºS: Results from two pilot boundary arrays in the South Atlantic. J. Geophys. Res., 118, 6461–6478, doi:10.1002/2013JC009228.

Meinen, C. S., Garzoli, S. L., Perez, R. C., Campos, E. J. D., Piola, A. R., Chidichimo, M. P., Dong, S. and Sato, O. T. (2017). Characteristics and causes of Deep Western Boundary Current transport variability at 34.5°S during 2009-2014. Ocean Sci., 13(1), 175, doi: 10.5194/os-13-175-2017.

Meinen, C. S., Speich, S., Piola, A. R., Ansorge, I. J., Campos, E. J. D., Kersalé , M., Terre, T., Chidichimo, M. P., Lamont, T., Sato, O. T., Perez, R. C., Valla, D., van den Berg, M. A., Le Hénaff, M., Dong, S., Garzoli, S. L. (submitted, 2018).

Meridional Overturning Circulation transport variability at 34.5°S during 2009-2017: Baroclinic and barotropic flows and the dueling influence of the boundaries. Geophys. Res. Lett.

Millot, C. and Taupier-Letage, I. (2005). Circulation in the Mediterranean sea. The Mediterranean Sea, 323-334.

Nelson, G., Boyd, A. J., Agenbag, J. J. and Duncombe Rae, C. M. (1998). An upwelling filament north-west of Cape Town, South Africa. Afr. J. Mar. Sci., 19(1), 75-88, doi: 10.2989/025776198784126953.

Olson, D. B. and Evans, R. H. (1986). Rings of the Agulhas current. Deep Sea Res., Part I, 33(1), 27-42, doi: 10.1016/0198-0149(86)90106-8.

Pallàs-Sanz, E., & Viúdez, Á. (2007). Three-dimensional ageostrophic motion in mesoscale vortex dipoles. J. Phys. Oceanogr., 37(1), 84-105, doi: 10.1175/JPO2978.1.

Pegliasco, C., Chaigneau, A. and Morrow, R. (2015). Main eddy vertical structures observed in the four major Eastern Boundary Upwelling Systems. J. Geophys. Res., 120(9), 6008-6033, doi:10.1002/2015JC010950.

Perez, R. C., Garzoli, S. L., Meinen, C. S. and Matano, R. P. (2011). Geostrophic velocity measurement techniques for the meridional overturning circulation and meridional heat transport in the South Atlantic. J. Atmos. Oceanic Technol., 28(11), 1504-1521, doi: 10.1175/JTECH-D-11-00058.1.

Piollé, J.-F. and Autret, E. (2011). Product user manual for ODYSSEA level 3 and 4 global and regional products, Proj. FP7-SPACE-2007-1, Ifremer, Issy-les-Moulineaux, France. Available at: http://projets.ifremer.fr/cersat/Data/Discovery/By-parameter/Sea-surface-temperature/ODYSSEA-Global-SST-Analysis.

Pujol, M. I., Faugère, Y., Taburet, G., Dupuy, S., Pelloquin, C., Ablain, M. and Picot, N. (2016). DUACS DT2014: the new multi-mission altimeter data set reprocessed over 20 years. Ocean Sci., 12(5), 1067-1090, doi: 10.5194/os-12-1067-2016.

Richardson, P. L., Lutjeharms, J. R. E. and Boebel, O. (2003). Introduction to the "Inter-ocean exchange around southern Africa". Deep Sea Res., Part I, 50(1), 1-12, doi: 10.1016/S0967-0645(02)00376-4.

Richardson, P. L. and Garzoli, S. L. (2003). Characteristics of intermediate water flow in the Benguela current as measured with RAFOS floats. Deep Sea Res., Part II, 50(1), 87-118, doi: 10.1016/S0967-0645(02)00380-6.

Robinson, A. R. (1983). Overview and summary of eddy science. In Eddies in marine science (pp. 3-15). Springer, Berlin, Heidelberg.

Roemmich, D. and Cornuelle, B. (1992). The subtropical mode waters of the South Pacific Ocean. J. Phys. Oceano., 22(10), 1178-1187, doi: 10.1175/1520-0485(1992)022<1178:TSMWOT>2.0.CO;2.

Roman, R. E. and Lutjeharms, J. R. E. (2007). Red sea intermediate water at the Agulhas current termination. Deep Sea Res., Part I, 54(8), 1329-1340, doi:10.1016/j.dsr.2007.04.009.

de Ruijter, W. P. M., Biastoch, A., Drijfhout, S. S., Lutjeharms, J. R. E., Matano, R. P., Pichevin, T., van Leeuwen, P. J. and Weijer, W. (1999). Indian-Atlantic interocean exchange: Dynamics, estimation and impact. J. Geophys. Res., 104(C9), 20885-20910, doi: 10.1029/1998JC900099.

de Ruijter, W. P., van Aken, H. M., Beier, E. J., Lutjeharms, J. R., Matano, R. P. and Schouten, M. W. (2004). Eddies and dipoles around South Madagascar: formation, pathways and large-scale impact. Deep Sea Res., Part I, 51(3), 383-400, doi: 10.1016/j.dsr.2003.10.011.

Rusciano, E., Speich, S. and Ollitrault, M. (2012). Interocean exchanges and the spreading of Antarctic Intermediate Water south of Africa. J. Geophys. Res., 117(C10), doi: 10.1029/2012JC008266.

Schiermeier, Q. (2013). Oceans under surveillance. Nature, 497(7448), 167-169.

Schouten, M. W., de Ruijter, W. P. M., van Leeuwen, P. J. and Lutjeharms, J. R. E. (2000). Translation, decay and splitting of Agulhas rings in the southeastern Atlantic Ocean. J. Geophys. Res., 105(C9), 21913–21925, doi: 10.1029/1999JC000046.

Spall, M. A. (1995). Frontogenesis, subduction, and cross-front exchange at upper ocean fronts. J. Geophys. Res., 100, 2543– 2557, doi: 10.1029/94JC02860.

Speich, S., et al. (2007). GOODHOPE/Southern Ocean: A study and monitoring of the Indotlantic connections. Mercator Newsletter, October 2007, 27, 29–41.

Speich, S., Garzoli, S., Piola, A. and the SAMOC community (2010). A monitoring system for the South Atlantic as a component of the MOC. In Proceedings of OceanObs'09: Sustained Ocean Observations and Information for Society (Annex), Venice, Italy, 21-25 September 2009, Hall, J., Harrison, D.E. & Stammer, D., Eds., ESA Publication WPP-306.

Sutherland, D. A., Straneo, F., Lentz, S. J. and Saint-Laurent, P. (2011). Observations of fresh, anticyclonic eddies in the Hudson Strait outflow. J. Mar. Syst., 88(3), 375-384, doi: 10.1016/j.jmarsys.2010.12.004.

Thomson, R. E. and Emery, W. J. (2014). Chapter 3 - Statistical Methods and Error Handling, In Data analysis methods in physical oceanography (Third Edition). Elsevier, Boston, 219-311 pp, doi: 10.1016/B978-0-12-387782-6.00003-X.

Ursella, L., Kovačević, V. and Gačić, M. (2011). Footprints of mesoscale eddy passages in the Strait of Otranto (Adriatic Sea). J. Geophys. Res., 116(C4), doi: 10.1029/2010JC006633.

Valla, D., Piola, A. R., Meinen, C. S. and Campos. E. (submitted, 2018). Strong mixing and recirculation in the northwestern Argentine Basin. J. Geophys. Res. Ocean.

Van Aken, H. M., Van Veldhoven, A. K., Veth, C., De Ruijter, W. P. M., Van Leeuwen, P. J., Drijfhout, S. S., Whittle, C. P. and Rouault, M. (2003). Observations of a young Agulhas ring, Astrid, during MARE in March 2000. Deep Sea Res., Part II, 50(1), 167-195, doi: 10.1016/S0967-0645(02)00383-1.

van Ballegooyen, R. C., Gründlingh, M. L. and Lutjeharms, J. R. (1994). Eddy fluxes of heat and salt from the southwest Indian Ocean into the southeast Atlantic Ocean: A case study. J. Geophys. Res., 99(C7), 14053-14070, doi: 10.1029/94JC00383.

van den Berg, M. A. (2015). Cruise report: SAMBA - Moorings and Monitoring Line, RS Algoa Voyage 221, 30 November - 6 December 2015. Department of Environmental Affairs Cruise Reports.

Van Sebille, E., England, M. H. and Froyland, G. (2012). Origin, dynamics and evolution of ocean garbage patches from observed surface drifters. Environ. Res. Lett, 7(4), 044040, doi: 10.1088/1748-9326/7/4/044040.

Watts, D. R., and H. Kontoyiannis (1990). Deep-ocean bottom pressure measurement: Drift removal and performance. J. Atmos. Oceanic Technol., 7(2), 296–306, doi:10.1175/1520-0426(1990)007<0296:DOBPMD>2.0.CO;2.

Watts, D. R., Sun, C. and Rintoul, S. (2001). A two-dimensional gravest empirical mode determined from hydrographic observations in the Subantarctic Front. J. Phys. Oceano., 31(8), 2186-2209, doi: 10.1175/1520-0485(2001)031<2186:ATDGEM>2.0.CO;2.

Whittle, C., Lutjeharms, J. R. E., Rae, D. and Shillington, F. A. (2008). Interaction of Agulhas filaments with mesoscale turbulence: a case study. S. Afr. J. Sci., 104(3-4), 135-139.

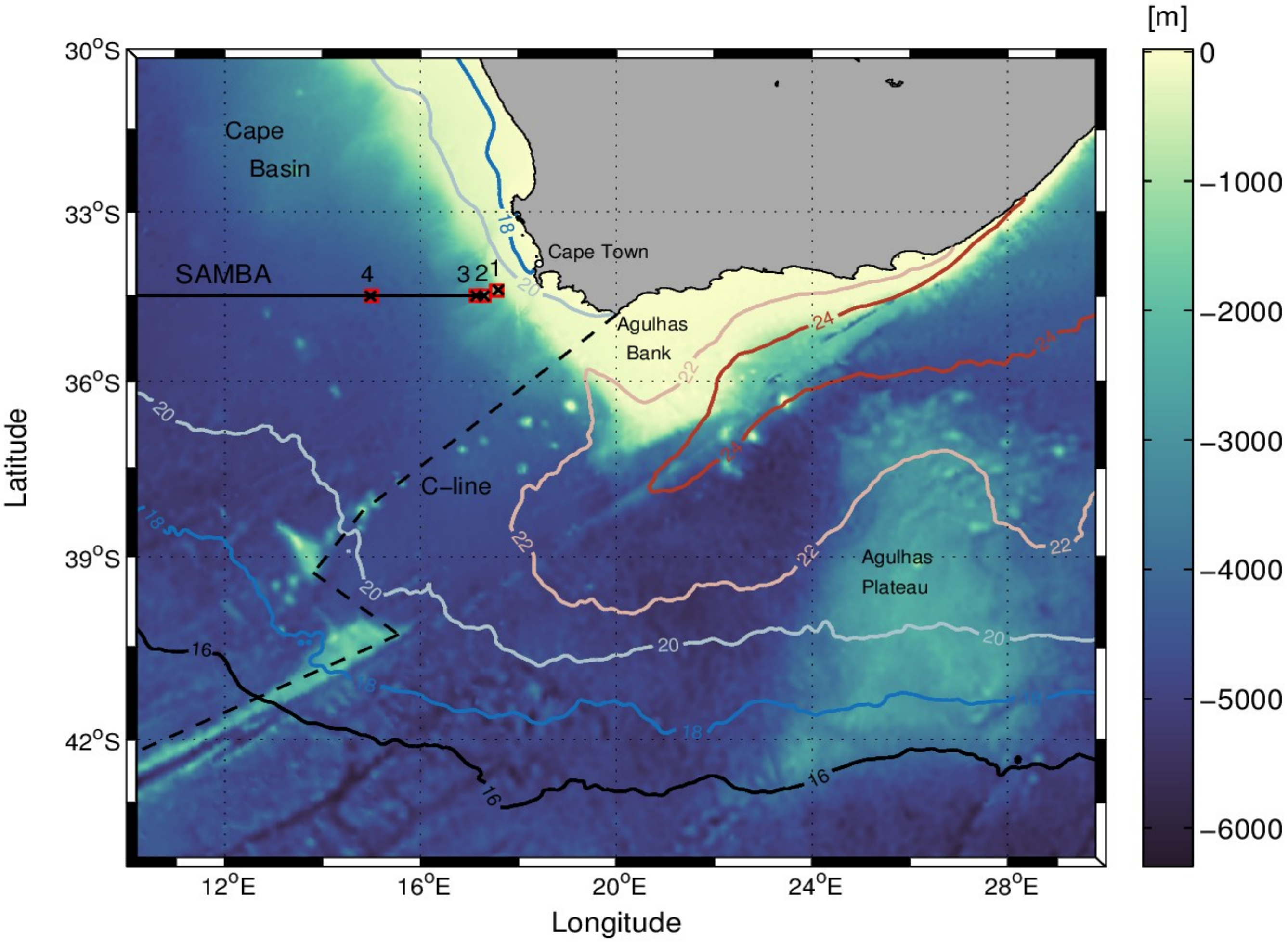

740 Figure 1: Study area with shaded color representing the bathymetry [m] from Etopo1. The thin black line denotes the position of the SAMBA-east line and the black crosses (red squares) represent the mooring (CPIES) positions with their associated numbers (1, 2, 3 and 4). The dotted black line denotes the C-line position from Laxenaire et al. (submitted, 2018). 2015 annual averaged SST isotherms from the ODYSSEA dataset are plotted with colored contours.

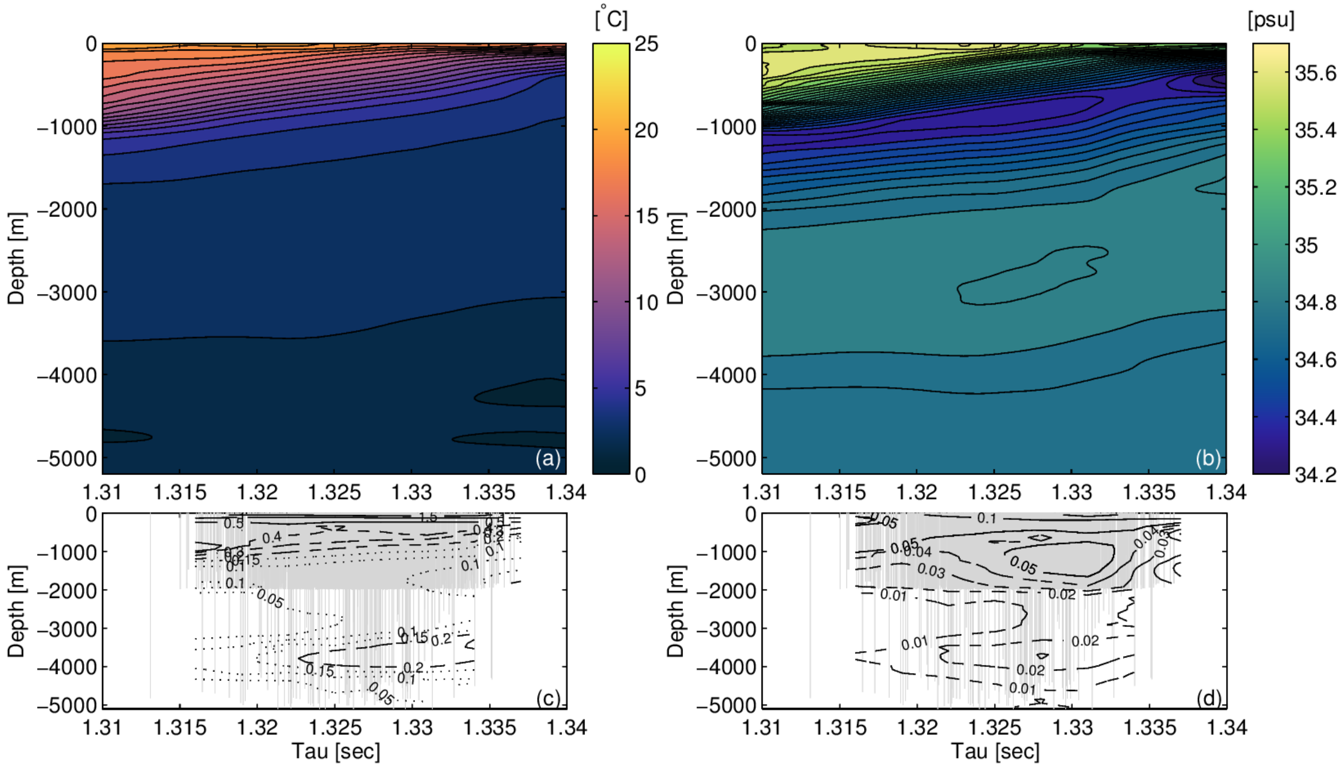

Figure 2: Gravest empirical mode (GEM) fields of temperature (a) and salinity (b) determined for the SAMBA-east line. The root-mean-squared (rms) differences between the original hydrographic measurements and the smoothed look-up table values are shown in the lower plots (c, d). The solid, dashed, and dotted contours represent progressively smaller contour intervals. The gray vertical lines show the locations of the hydrographic measurements. 745

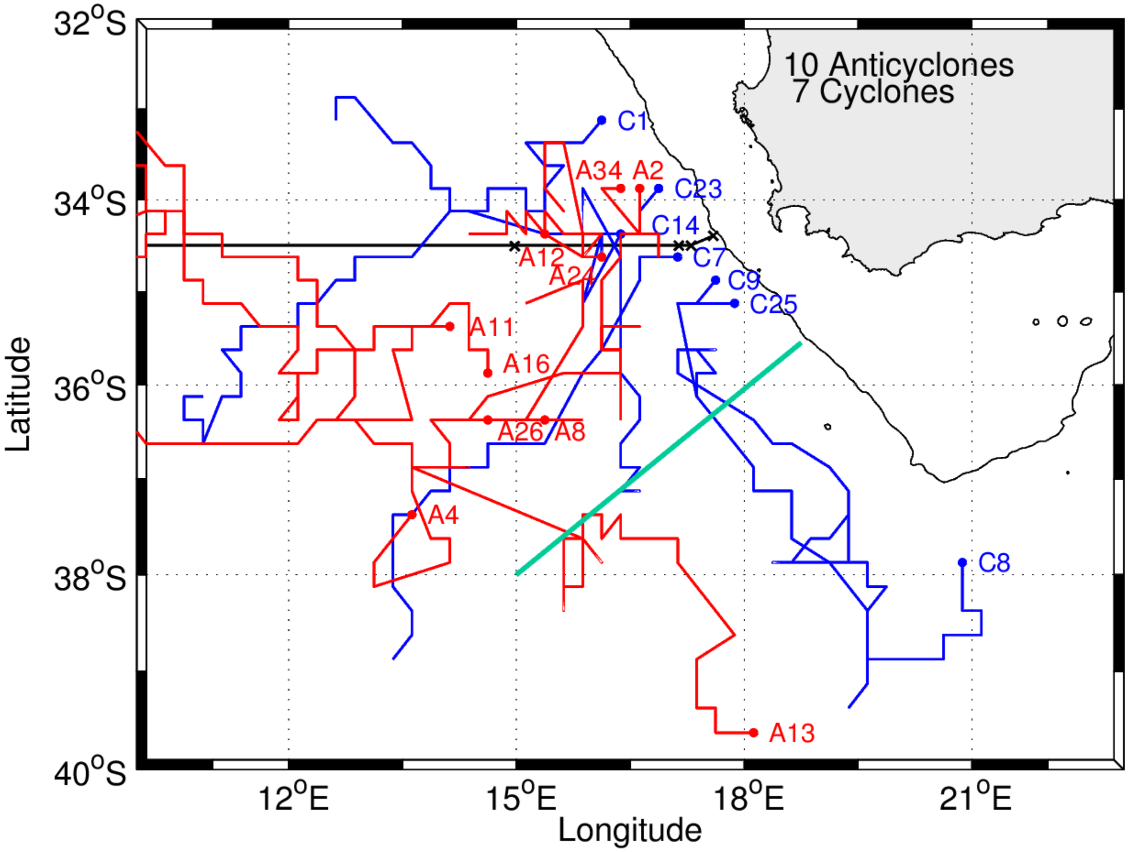

Figure 3: Eddy trajectories from September 15, 2014 to December 15, 2015 for eddies influencing the moorings measurements. The eddies are named as CN (cyclonic eddies) and AN (anticyclonic eddies), with N a number assigned in chronological order by the eddy tracking scheme. The red lines are trajectories of anticyclonic eddies and blue lines trajectories of anticyclonic eddies. The circles indicate the starting positions of an eddy track . The green line represents the northern route of Agulhas rings defined by Dencause et al. (2010).

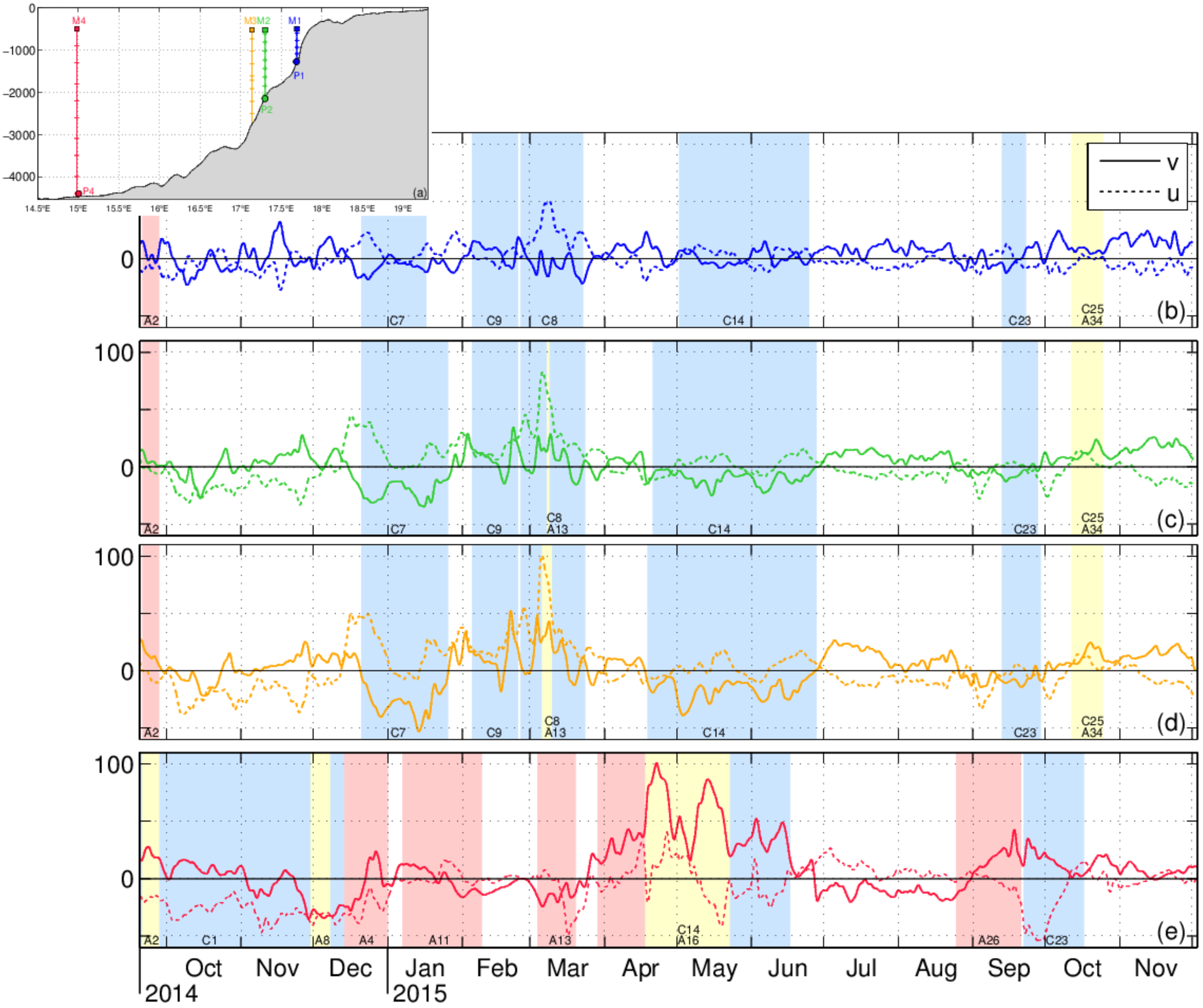

Figure 4: (a) Vertical scheme of the mooring lines positions along the latitude 34.5°S. The squares represent the upward-looking ADCP positions, the small horizontal lines indicate the SBE Microcat's sensors and the circles at the bottom show the CPIES. Temporal evolution of the depth-averaged u (dashed line) and v (solid line) component of the current velocity at M1 (b - blue line), M2 (c - green line), M3 (d - blue line) and M4 (e - red line) [cm s^{-1}]. The shaded areas show the eddy events defined with altimetry data (red: anticyclonic eddies, yellow: dipole events and blue: cyclonic eddies).

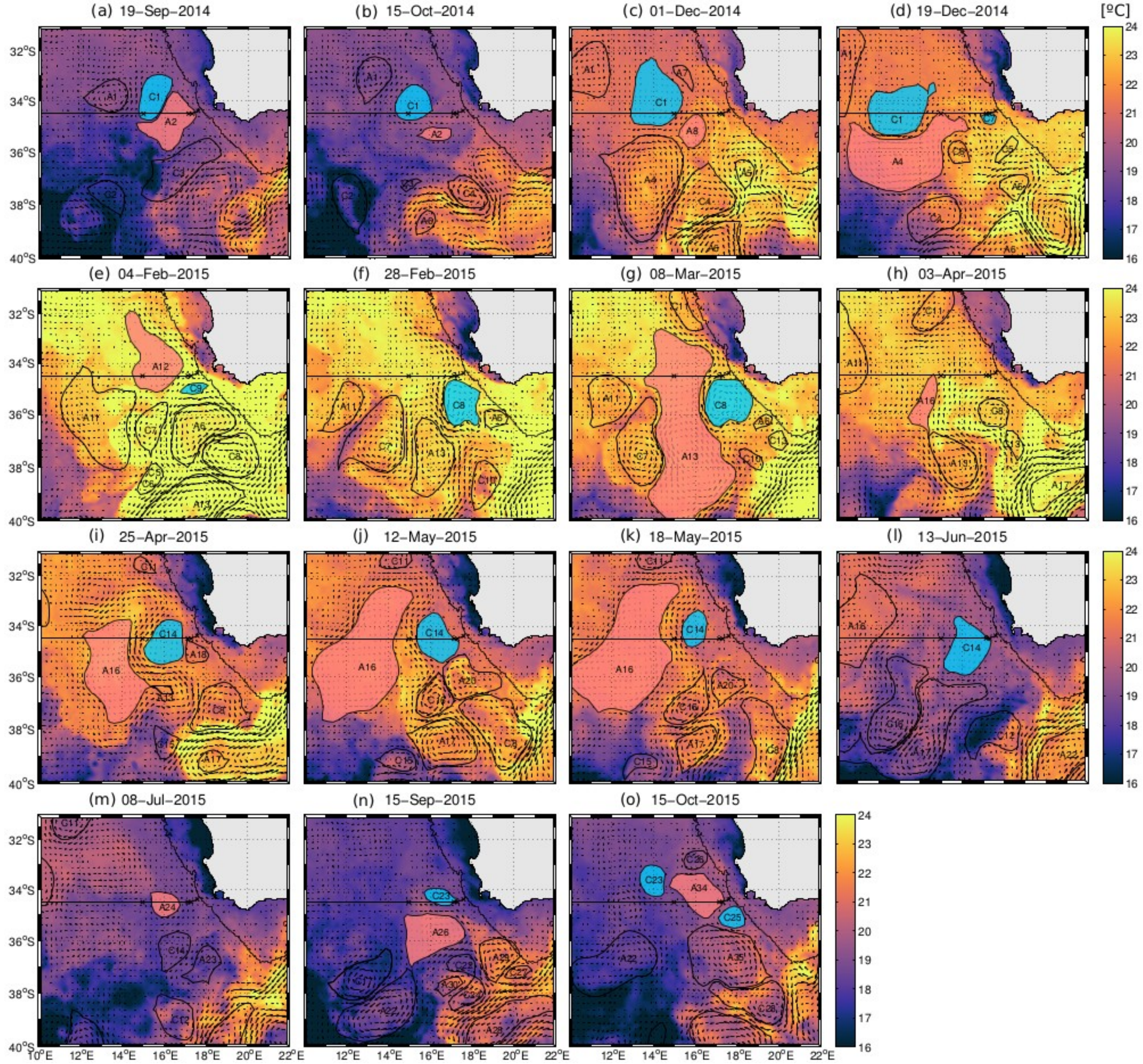
(a) 19-Sep-2014 (b) 15-Oct-2014 (c) 01-Dec-2014 (d) 19-Dec-2014
(e) 04-Feb-2015 (f) 28-Feb-2015 (g) 08-Mar-2015 (h) 03-Apr-2015
(i) 25-Apr-2015 (j) 12-May-2015 (k) 18-May-2015 (l) 13-Jun-2015
(m) 08-Jul-2015 (n) 15-Sep-2015 (o) 15-Oct-2015

Figure 5: SST satellite images for selected dates between September 19, 2014 to October 15, 2015. The black line denotes the position of the SAMBA line and the crosses represent the mooring positions. Black contours show the eddies identification. The colored eddies (red for AN and blue for CN) are identified as close enough to affect the measurement at the different moorings.

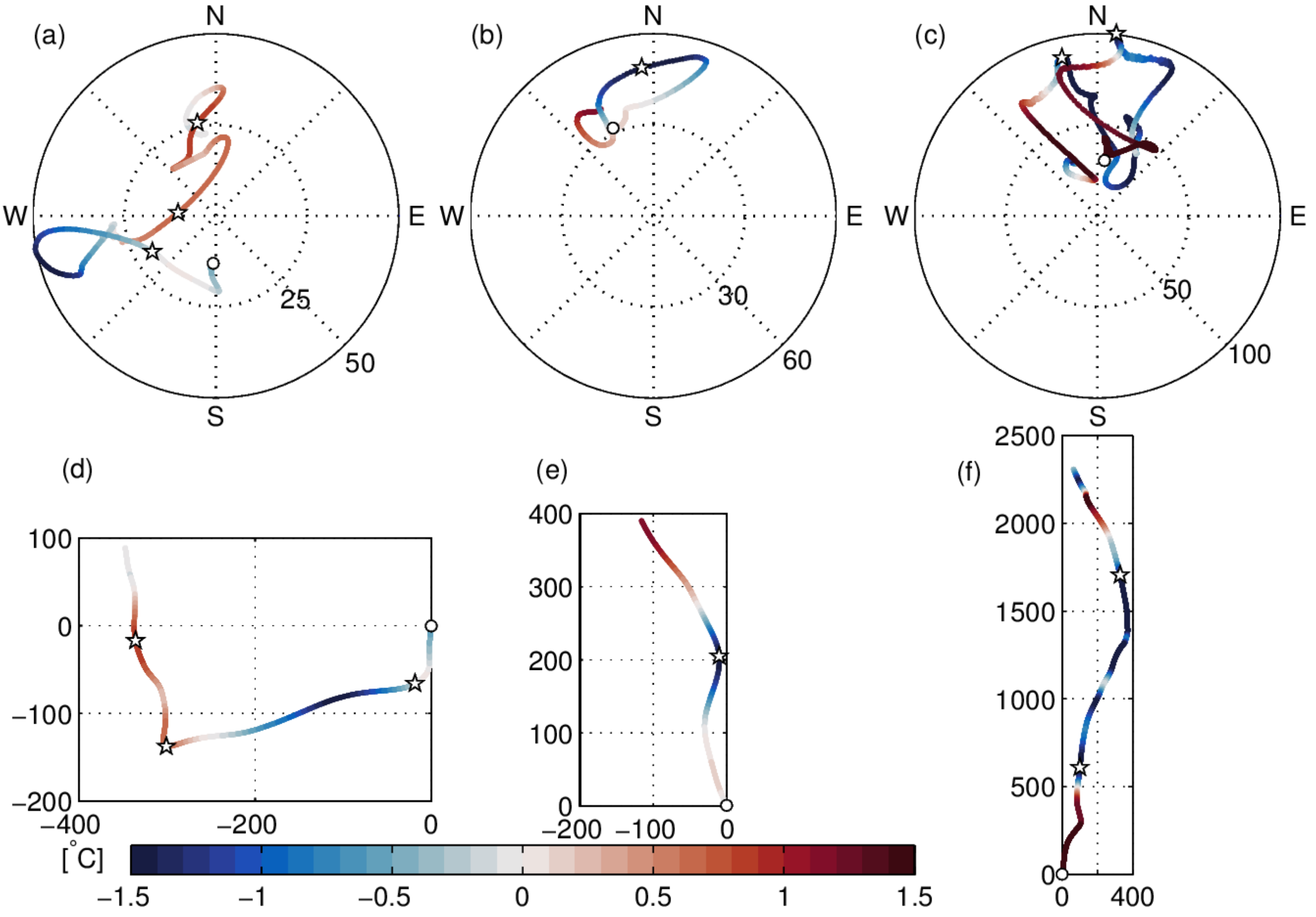

Figure 6: (a, b, c) Hodograph of the mean currents of the upper-water column observed at M4 for three case studies (a- Anticyclonic eddies and filament; b- Cyclonic eddy; c- Dipole). Color represents the temperature recorded at the first SBE37 Microcat's demeaned over the time period of each case studies (a: March 9 – April 6, 2015; b: May 28 – June 10, 2015; c: April 8 – May 29, 2015). The estimated centers of 6 events have been marked with white stars. The beginning of each time series has been marked with white dote. (d, e, f) Progressive vector diagram for the mean currents of the upper-water column observed at M4 for three case studies. Color, time period and symbols are the same than the hodograph.

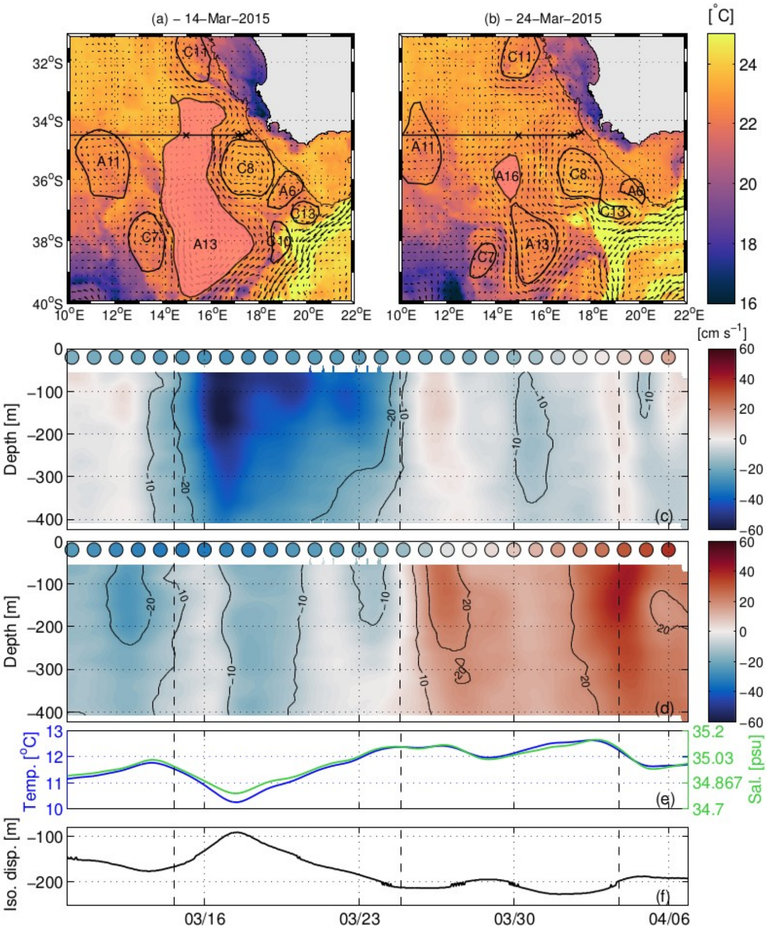

Figure 7: #Anticyclonic eddy: (a, b) SST satellite images for selected dates (vertical black lines on the time series). Vertical-temporal section of the u-component (c) and v-component (d) of the current speed measured from the upward-looking ADCP at M4. The colored circles at the top of the section show the u-component and v-component of the current speed from altimetry data. (e) Temporal evolution of temperature (blue line) and salinity (green line) and (f) the isopycnal displacement recorded at the 500 m depth SBE37 Microcat's.

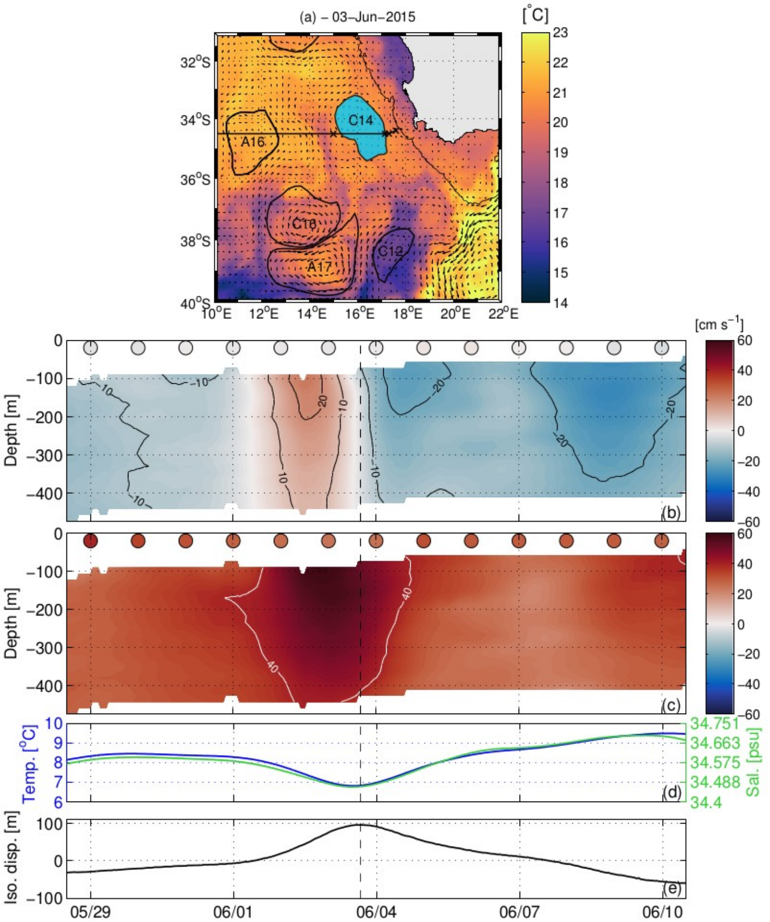

Figure 8: #Cyclonic eddy: (a) SST satellite images for selected date (vertical black lines on the time series). Vertical-temporal section of the u-component (b) and v-component (c) of the current speed measured from the upward-looking ADCP at M4. The colored circles at the top of the section show the u-component and v-component of the current speed from altimetry data. (d) Temporal evolution of temperature (blue line) and salinity (green line) and (e) the isopycnal displacement recorded at the 500 m depth SBE37 Microcat's.

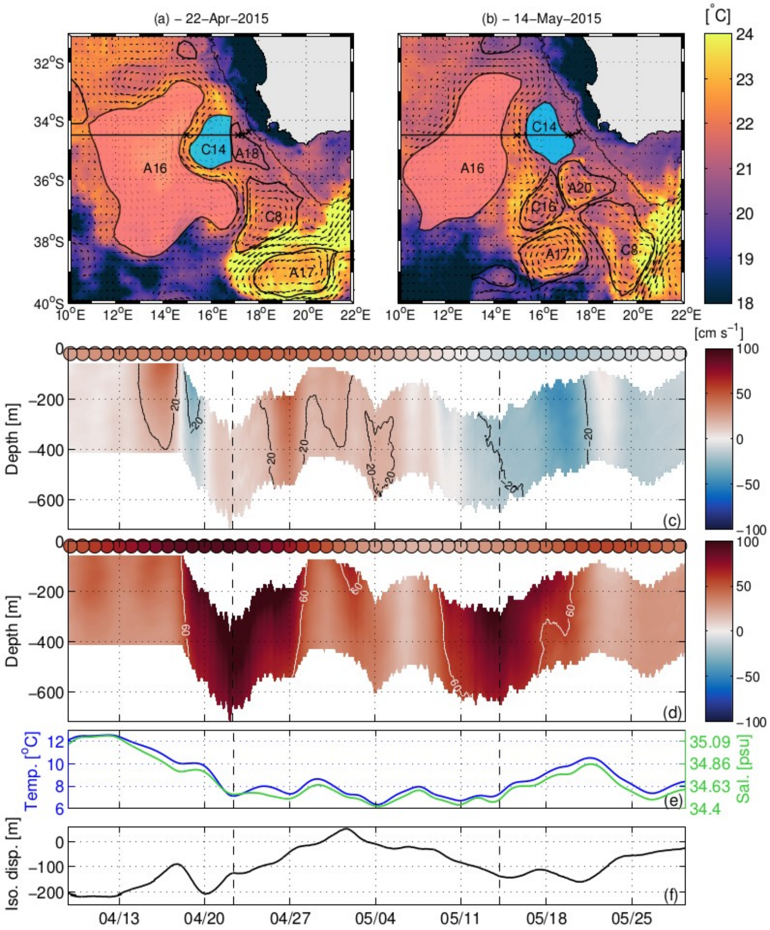

Figure 9: #Intrusion water: (a, b) SST satellite images for selected dates (vertical black lines on the time series). Vertical-temporal section of the u-component (c) and v-component (d) of the current speed measured from the upward-looking ADCP at M4. The colored circles at the top of the section show the u-component and v-component of the current speed from altimetry data. (e) Temporal evolution of temperature (blue line) and salinity (green line) and (f) the isopycnal displacement recorded at the 500 m depth SBE37 Microcat's.

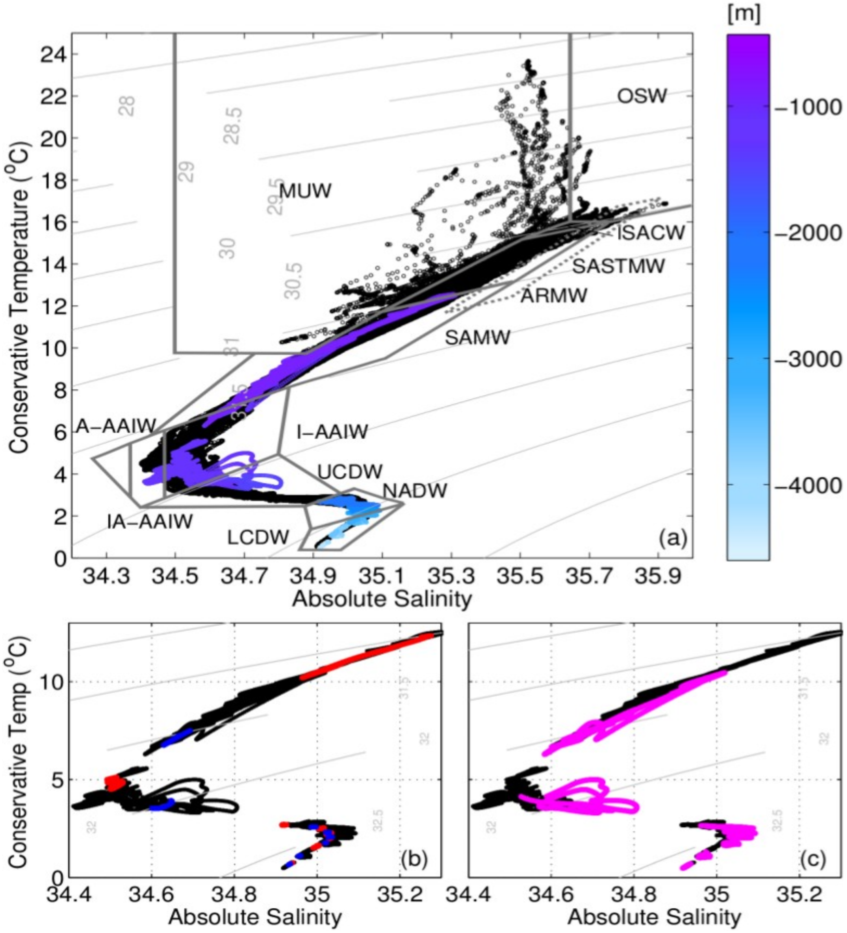

Figure 10: (a) Conservative Temperature (°C) – Absolute Salinity (g kg^{-1}) relationship from the hydrographic cruises sampling along the SAMBA-east array (black dots) and from the SBE37 MicroCATs colored dots with their associated depth. Water masses are indicated by gray boxes (OSW – Oceanic Surface Water, MUW – Modified Upwelled Water, lSACW – Light South Atlantic Central Water, SASTMW – South Atlantic Subtropical Mode Water, SAMW – Subantarctic Mode Water, ARMW – Agulhas Ring Mode Water, I-AAIW – Indian Antarctic Intermediate Water, IA-AAIW – Indo-Atlantic Antarctic Intermediate Water, A-AAIW – Atlantic Antarctic Intermediate Water, UCDW – Upper Circumpolar Deep Water, NADW – North Atlantic Deep Water, and LCDW – Lower Circumpolar Deep Water). (b,c) Same relationship from the SBE37 MicroCATs. The colored dots represent the water masses associated to each case studies (#Anticyclonic eddies: red, #Cyclonic eddy: blue, #Dipole intrusions: magenta).

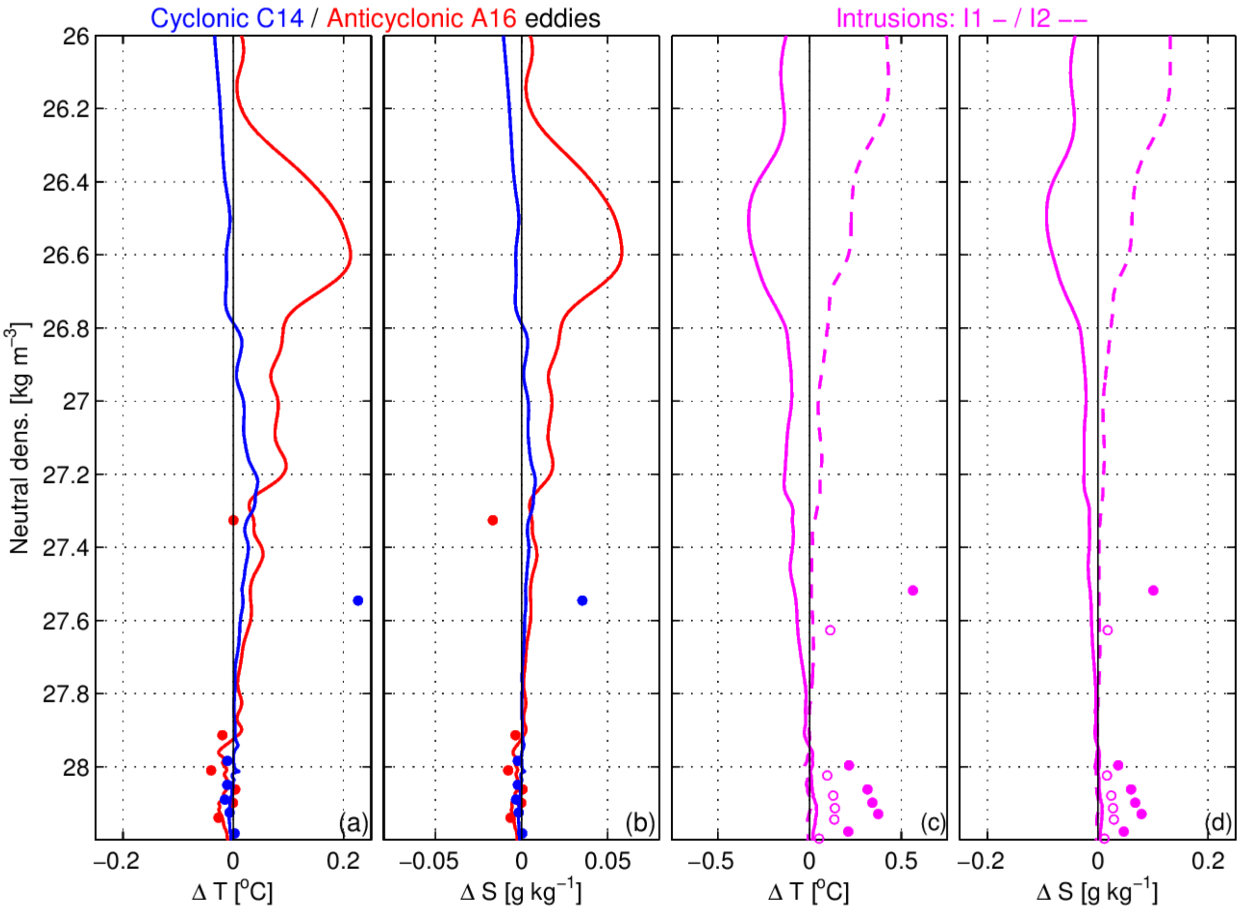

Figure 11: Vertical profiles of the conservative temperature (a,c) and absolute salinity (b,d) anomalies at M4 due to the presence of the #Anticyclonic eddy; #Cyclonic eddy (a,b) and the two intrusions associated with the dipole (c,d). The colored dots represent the value from the SBE37 Microcat's and the solid or dashed lines from the reconstructed GEM fields. The magenta colored dotes and the solid line are associated to the first intrusion (I1); the colored circles and the dashed lines for the second intrusion (I2).

Table I: Moorings and CPIES characteristics.

	Mooring 1 - M1	Mooring 2 - M2	Mooring 3 - M3	Mooring 4 - M4
Latitude	34ºS 23.636'	34ºS 29.960'	34ºS 30.010'	34ºS 30.360'
Longitude	17ºE 35.664'	17ºE 18.064'	17ºE 8.3640	14ºE 58.810'
Water depth (m)	1121	2094	2970	4474
Start	17/09/2014 08:00	17/09/2014 11:00	17/09/2014 16:00	19/09/2014 23:00
End	01/12/2015 05:00	01/12/2015 13:00	02/12/2015 10:00	03/12/2015 05:00
ADCP	75kHZ RDI ADCP	75kHZ RDI ADCP	75kHZ RDI ADCP	75kHZ RDI ADCP
Depth (m)	600	605	435	450
Cell size (m)	16	16	16	16
Number bins	34	34	24	24
Depth 1st bin (m)	582.85	588.65	410.95	413.78
Ensemble lengths	10 558	10 566	10 587	10 606
Depth (m) SBE 37 SMP MicroCat's C-T (***P***) Recorder	***600***, 770, ***930***, 1090	***605***, 810, 1020, 1230, 1435, 1642, 1850, 2070	***435***, 730, 1030,1325, 1620, 1720, 1915, 2210, 2505, 2880	***450***, 895, 1340, 1780, 2250, 2665, 3110, 3550, 3985, 4360

	CPIES 1 - P1	CPIES 2 - P2	CPIES 3 - P3	CPIES 4 - P4
Latitude	34ºS 24.348'	34ºS 29.813'	34ºS 29.964'	34ºS 30.252'
Longitude	17ºE 33.456'	17ºE 18.036'	17ºE 8.3100'	15ºE 0.161'
Water depth (m)	1266	2129	2850	4482
Start	07/09/2013 00:00	07/09/2013 00:00	No data	07/09/2013 00:00
End	11/08/2015 00:00	11/08/2015 00:00	No data	11/08/2015 00:00

Table II: Summary of comparison statistics for satellite altimetry and moored current meter, with R the correlation coefficient, ΔV_{rms} the root mean square differences between the zonal and meridional components of ADCPs and those from altimetry (Eq. 1), and the bias between those components (Eq. 2).

	R		ΔV_{rms} [cm s^{-1}]		Bias [cm s^{-1}]	
	u	v	u	v	u	v
M1 (54.9 m)	0.32	0.30	15.4	13.3	5.3	-1.5
M2 (60.7 m)	0.72	0.59	14.0	12.9	3.0	-8.8
M3 (43.0 m)	0.81	0.67	13.3	13.9	-5.8	1.2
M4 (45.8 m)	0.80	0.83	13.0	15.9	-4.3	-4.9

Table III: Characteristics of the eddies passing over the moorings from satellite altimetry. The time period, the radius and the azimuthal velocity of the different eddies are derived from the eddy detection method. The eddies are named as CN (cyclonic eddies) and AN (anticyclonic eddies), with N a number assigned in chronological order by the eddy tracking scheme. Eddies generate at the Agulhas retroflection are identified with a star.

Δt [days] Radius [km] max(V) [cm s-1]	C1	C7	C9	C8*	C14	C23	C25
M1, M2, M3		28-37 49.6 -36.0	20 39.1 -38.4	28 100.2 -66.3	55-71 92.0 -40.9	11-17 61.9 -25.7	14 50.6 -33.5
M4	93 98.3 -34.1				61 89.9 -42.7	26 85.3 -21.0	

Δt [days] Radius [km] max(V) [cm s-1]	A2	A4	A8	A11	A12	A13*	A16	A24	A26	A34
M1,M2, M3	8 120.1 21.7					2-5 241.7 60.7				1 100.4 22.8
M4		19 178.5 53.9	9 59.6 39.8	34 135.9 33.4	1 102.2 21.2	17 204.0 58.6	56 182.0 37.2	1 81.09 17.2	28 113.6 51.1	

Table IV: Estimate eddy parameters: t0: the eddy's center apparent at M4, Δt: temporal half eddy duration, $U/\Theta_{a/f}$ ($X_{a/f}$): the estimated mean flow magnitude and direction (eddy apparent radius) using the angle method (subscript “a”) or the filtering method (subscript “f”). V_n/V_U: the estimated maximum eddy currents using the normal (subscript “n”) or the U subtraction method (subscript “U”). Rossby number using the different value for V and X.

	A13	A16	C14
t0	March 14, 2015 - 3pm	March 24, 2015 - 9pm	June 3, 2015 - 4pm
Δt [h]	54	48	25
U_a [cm s^{-1}]	27.0	18.3	50.7
Θ_a	110	77	2
U_f [cm s^{-1}]	28.9	16.5	49.5
Θ_f	150	77	2
V_n [cm s^{-1}]	25.8	20.6	-19.2
V_U [cm s^{-1}]	26.0	21.7	-20.0
X_a [km]	52.4	31.6	45.7
X_f [km]	56.2	28.4	44.5
Rossby number	0.11-0.12	0.15-0.17	0.10

Table V: Table with the different water masses and their definition in terms of conservative temperature, absolute salinity and density layers.

Water mass		Definition
MUW		$9.71 \leq T \leq 21.3°C$; $34.661 \leq S_A \leq 35.647$ g kg^{-1}
OSW		$\gamma^n < 26.2$ kg m^{-3}; $T \geq 16.0°C$; $S_A \geq 35.647$ g kg^{-1}
lSACW		$15.15 \leq T \leq 16°C$; $35.506 \leq S_A \leq 35.764$ g kg^{-1}
SASTMW		$11.69 \leq T \leq 16°C$; $35.49 \leq S_A \leq 35.764$ g kg^{-1}
SAMW		$6.32 \leq T \leq 13.18°C$; $34.78 \leq S_A \leq 35.49$ g kg^{-1}
ARMW		$11.60 \leq T \leq 17.00°C$; $35.18 \leq S_A \leq 35.81$ g kg^{-1}
AAIW	I-AAIW	$S_A \geq 34.47$ g kg-1
	IA-AAIW	$34.37 \leq S_A \leq 34.47$ g kg-1
	A-AAIW	$S_A \leq 34.37$ g kg-1
UCDW		$27.55 < \gamma^n < 27.92$ kg m^{-3}; $T < 4.23°C$; $34.696 \leq S_A \leq 35.916$ g kg^{-1}
NADW		$27.92 < \gamma^n < 28.11$ kg m^{-3};
LCDW		$28.11 < \gamma^n < 28.26$ kg m^{-3};